Diverse Lava Flow Morphologies in the Stratigraphy of the Jezero Crater Floor

S. Alwmark, B. Horgan, A. Udry, A. Bechtold, S. Fagents, E. Ravanis, L. Crumpler, N. Schmitz, E. Cloutis, A. Brown, et al.

Diverse Lava Flow Morphologies in the Stratigraphy of the Jezero Crater Floor

S. Alwmark[1,2], B. Horgan[3], A. Udry[4], A. Bechtold[5], S. Fagents[6], E. Ravanis[6], L. Crumpler[7], N. Schmitz[8], E. Cloutis[9], A. Brown[10], D. Flannery[11], O. Gasnault[12], J. Grotzinger[13], S. Gupta[14], L. Kah[15], P. Kelemen[16], K. Kinch[1], and J. Núñez[17]

[1]Department of Geology, Lund University, Lund, Sweden. [2]Niels Bohr Institute, University of Copenhagen, Copenhagen, Denmark. [3]Department of Earth, Atmospheric, and Planetary Sciences, Purdue University, West Lafayette, IN, USA. [4]Department of Geoscience, University of Nevada Las Vegas, Las Vegas, NV, USA. [5]Austrian Academy of Sciences, Vienna, and University of Vienna, Department of Lithospheric Research, Vienna, Austria. [6]Hawai'i Institute of Geophysics and Planetology, University of Hawai'i at Mānoa, Honolulu, HI, USA. [7]New Mexico Museum of Natural History & Science, Albuquerque, NM, USA. [8]German Aerospace Center (DLR), Institute of Planetary Research, Berlin, Germany. [9]The University of Winnipeg, Winnipeg, Manitoba, Canada. [10]Plancius Research, Severna Park, MD, USA. [11]Queensland University of Technology, Brisbane, Queensland, Australia. [12]Institut de Recherche en Astrophysique et Planétologie (IRAP), Université de Toulouse, CNRS, CNES, Toulouse, France. [13]Division of Geological and Planetary Sciences, Caltech, Pasadena, CA, USA. [14]Department of Earth Science & Engineering, Imperial College London, London, UK. [15]Department of Earth and Planetary Sciences, University of Tennessee-Knoxville, Knoxville, TN, USA. [16]Department of Earth & Environmental Sciences, Columbia University, Palisades, NY, USA. [17]Johns Hopkins University Applied Physics Laboratory, Laurel, MD, USA.

Corresponding author: Sanna Alwmark (sanna.alwmark@geol.lu.se)

Key Points:

- We investigated Artuby and Rochette member rocks of the Máaz formation in Jezero crater using *Perseverance's* Mastcam-Z and SuperCam data.
- Complex knobbly, foliated, vesicular, and layered lithologies are most consistent with lava flows originating through multiple eruptions.
- The Máaz formation in Jezero crater could be unrelated to the regional Circum–Isidis capping unit.

Abstract

We present a combined geomorphologic, multispectral, and geochemical analysis of crater floor rocks in Jezero crater based on data obtained by the Mastcam-Z and SuperCam instruments onboard the NASA Mars 2020 *Perseverance* rover. The combined data from this analysis together with the results of a comparative study with geologic sites on Earth allows us to interpret the origins of rocks exposed along the Artuby ridge, a ~900 m long scarp of lower Máaz formation rocks. The ridge exposes rocks belonging to two morphologically distinct members, Artuby and Rochette, that both have basaltic composition and are spectrally indistinguishable in our analysis. Artuby rocks consist of morphologically distinct units that alternate over the ridge, bulbous, hummocky, layers with varying thicknesses that in places appear to have flowed over underlying strata, and sub-planar thinner laterally continuous layers with variable friability. The Rochette member has a massive appearance with pronounced pitting and sub-horizontal partings. Our findings are most consistent with a primary igneous emplacement as lava flows, through multiple eruptions, and we propose that the thin layers result either from preferential weathering, interbedded ash/tephra layers, ʻaʻā clinker layers, or aeolian deposition. Our analyses provide essential geologic context for the Máaz formation samples that will be returned to Earth and highlight the diversity and complexity of geologic processes on Mars not visible from orbit.

Plain Language Summary

Characterization of the landing site for the Mars 2020 *Perseverance* rover mission yields insight into early solar system processes and provides essential context for Mars Sample Return. Here we have investigated crater floor rocks in Jezero crater that are exposed along a scarp called Artuby ridge with the Mastcam-Z and SuperCam instruments onboard the *Perseverance* rover. The Artuby ridge displays a characteristically layered set of rocks with a basaltic composition that are spectrally and chemically indistinguishable in our investigation. We compare our observations from Jezero with well-understood geologic deposits on Earth, from Hawai‘i and New Mexico. We find that terrestrial lava flows can have complex interiors that replicate many features that we see in Mastcam-Z images of the Artuby ridge, and thus, that the series of rocks exposed along the Artuby ridge are dominated by lava flows originating through multiple eruptions. There are a number of layers and textures of the rocks in our investigation that may not have originated as lava flows, that instead may be products of weathering, interbedding of lava and volcanic ash/tephra, or wind-borne sediment deposition. Our results highlight the diversity of geologic units on Mars not visible from orbit.

1 Introduction

The NASA Mars 2020 *Perseverance* rover landed in Jezero crater on February 18th, 2021 (Fig. 1a,b). Jezero crater is ~45 km in diameter and located in the Nili Fossae region, on the northwestern margin of the ~1200 km-diameter Isidis impact basin. The formation age of Jezero crater can be bracketed by the formation of the Isidis basin (3.96 ± 0.01 Ga; Werner, 2008; or 4.05–4.20 Ga; Marchi et al., 2021) and emplacement of the crater rim-draping regional olivine- and carbonate-bearing unit (3.82 ± 0.07 Ga; Goudge et al., 2015; Mandon et al., 2020). This places its formation in the Noachian period, which was a warmer and wetter period of Mars history (e.g., Irwin et al., 2005; Kite, 2019; Palumbo et al., 2020; Salese et al., 2020). The crater once hosted an open-basin lake fed by a valley network bringing in sediments that built the

prominent western delta (e.g., Fassett & Head, 2005, 2008a,b; Goudge et al., 2015, 2017; Mangold et al., 2020, 2021; Schon et al., 2012). *Perseverance* is tasked with characterizing the geology of the landing site, evaluating the astrobiological potential of recorded geologic environments, and selecting, collecting, and documenting a set of in situ samples (Farley et al., 2020).

The shallow depth profile of Jezero crater indicates substantial crater-fill with an estimated thickness of ~1 km (Ehlmann et al., 2008; Garvin et al., 2003; Schon et al., 2012). Orbital mapping of the exposed geologic units on the Jezero crater floor prior to landing (Stack et al., 2020) highlights three major crater filling materials: Crater Floor Fractured Rough (Cf-fr) and Crater Floor Fractured 1 and 2 (Cf-f-1, Cf-f-2). Studies previous to the Stack et al. (2020) mapping effort did not distinguish Cf-f-1 and Cf-f-2 as two separate units, due to their similar morphological and spectral signatures. The separation in Stack et al. (2020) is based on subtle differences in surface texture between the two units, and on elevation, where Cf-f-2 crops out at higher elevation inside the crater. During the crater floor campaign of the Mars 2020 mission *Perseverance* traversed over Cf-fr and Cf-f-1 (see Sun et al., 2022; Sun et al., this issue). Cf-f-1 is stratigraphically lower than Cf-fr (Farley et al., 2022; Sun et al., 2022; Sun et al., this issue), and has a distinct olivine-like signature in near-infrared (NIR) reflectance spectra, whereas the younger Cf-fr displays NIR reflectance-spectra more indicative of pyroxene (Horgan et al., 2020). In situ analysis by *Perseverance* confirms that Cf-fr, which has informally been named the Máaz formation, is dominated by augite and plagioclase, and Cf-f-1, the Séítah formation, consists of olivine, augite, and plagioclase (Bell et al., 2022; Farley et al., 2022; Liu et al., 2022; Núñez et al., 2022; Schmidt et al., 2022; Udry et al., this issue; Udry et al., 2022). Preflight analysis based on orbital data (Brown et al., 2020; Goudge et al., 2012, 2015; Kremer et al., 2019; Mandon et al., 2020) suggests that Cf-f-1 (and Cf-f-2) is genetically related to the regional olivine-bearing unit, either as simply a part of that unit, or as material from the regional unit eroded, transported, and redeposited within Jezero. Based on in situ data from *Perseverance*, Farley et al. (2022), Liu et al. (2022), and Wiens et al. (2022) interpret the Séítah formation as a slowly cooled olivine cumulate emplaced as a thick lava flow, lava lake, or intrusion, which is inconsistent with fluvial reworking and is difficult to reconcile with Séítah being simply a part of the regional unit, as that would imply a huge volume of regionally spread, slowly-cooling, ultramafic melt.

Characterizing the crater floor rocks in Jezero crater is essential for constraining processes that acted during early Martian history and for documenting context for Mars sample return. During sols 169–200 of the *Perseverance* mission, the rover traversed east-to-west along the contact between the underlying Séítah (Cf-f1) and the overlying Máaz (Cf-fr) formations, where an exposed scarp along the contact was named the *Artuby ridge*. During sols 285–351 the rover traversed back west-to-east along the same contact. In this contribution, we present detailed descriptions of Máaz formation rocks exposed along the Artuby ridge, and discuss the genesis of rocks described in this setting.

Decades of studies of Mars with orbital instruments, landers, and rovers have revealed a diverse geologic history, that in many aspects is Earth-like (e.g., Carr, 2018). Given the wealth of complex and interconnected geologic processes recorded, such as fluvial and glacial activity, impact processes, igneous processes, and crustal tectonic activity, comparison with known, or more well-understood, terrestrial geologic processes guides our understanding of geologic processes on Mars. Terrestrial analog sites are thus widely accepted as a key source of information in understanding processes that have shaped and modified the geologic history of

Mars (e.g., Farr, 2004; see also papers in Chapman, 2007). In this work, we use relevant sites on Earth as a reference to interpret data obtained with *Perseverance*. Here we answer the questions: What features of the Artuby ridge can we resolve in Mast Camera Zoom (Mastcam-Z) images? How do these features and textures compare to Earth analogs? Can we use our observations to constrain the origin of these rocks?

2 The Máaz formation

The Máaz formation dominates the crater floor in Jezero crater. It has lobate margins that appear to embay topographically higher regions. Several authors have hypothesized that the Máaz formation (Cf-fr unit) in Jezero and a unit mapped outside of the crater, the Nili plains 2 unit (Sun & Stack, 2020a,b) or mafic capping unit (Bramble et al., 2017), have a common history (see also Hundal et al., 2022; Sun & Stack, 2020a). Prior to landing, a series of publications hypothesized that the Máaz formation originated as a lava flow (e.g., Goudge et al., 2012, 2015; Schon et al., 2012), or that it had a fluviolacustrine or aeolian origin (Holm-Alwmark et al., 2021; Kah et al., 2020; Shahrzad et al., 2019; Stack et al., 2020; see also discussion in Horgan et al., 2020 and Sun & Stack 2020b). However, surveys in Jezero crater have shown that the crater floor rocks investigated up close with the SuperCam, Planetary Instrument for X-ray Lithochemistry (PIXL), Scanning Habitable Environments with Raman & Luminescence for Organics & Chemicals (SHERLOC), and Wide Angle Topographic Sensor for Operations and eNgineering (WATSON) instruments are igneous, based on the holocrystalline interlocking texture, mineralogy, and bulk composition (Farley et al., 2022; Liu et al., 2022; Sun et al., 2022; Schmidt et al., 2022; Udry et al., 2022). As the unit is crater retaining, it holds great potential as an anchor for calibrating crater chronology if its age can be determined with returned samples (e.g., Herd et al., 2021; Simon et al., this issue; Simon et al., 2022).

The Máaz formation also has the potential to constrain processes such as fluvial activity inside Jezero crater. Various publications have proposed cases for the relative timing of deposition of the dominant geomorphologic units in the *Perseverance* vicinity (i.e., the western delta, Cf-fr, and Cf-fl), with scenarios presented for Cf-fr deposition before delta formation (Holm-Alwmark et al., 2021; Horgan et al., 2020; Ruff, 2017; Stack et al., 2020; Sun & Stack, 2020a), after delta formation (Goudge et al., 2015; Schon et al., 2012; Stack et al., 2020), and interfingering delta/crater floor rocks (e.g., Horgan et al., 2022; Stack et al., 2020).

The Máaz formation is morphologically diverse, consisting of blocky, massive, pitted, and layered rocks, and has been subdivided (descending stratigraphically) into the Ch'ał, Naat'áanii, Roubion, Rochette, and Artuby members (Crumpler et al., this issue; Horgan et al., this issue; Sun et al., 2022; Sun et al., this issue). The Ch'ał member is seemingly massive, forms blocky terrains (Horgan et al., 2022; Sun et al., 2022), and was traversed near the landing site. The blocky terrain forms the rough surface texture of parts of the crater floor located east of the Octavia E. Butler (OEB) landing site in Jezero (Fig. 1c). Flat-lying polygonally fractured rocks of the Naat'áanii and Roubion members were traversed on the way from OEB to the Artuby ridge. The other members were first observed at or near the Artuby ridge (see below). Roubion rocks were interpreted by Farley et al. (2022) as the lowest stratigraphical exposure of the Máaz formation, overlain by the Artuby member near the Artuby ridge and by the Rochette member just south of OEB. Later interpretations by Horgan et al. (this issue) interpret Roubion to be

intermediate stratigraphically between lower (the Artuby and Rochette members) and upper (the Naat'áanii and Ch'ał members) Máaz, at least near the OEB landing site (Fig. 1d).

The upper Máaz formation rocks of Ch'ał and Naat'áanii exhibit Mastcam-Z spectra consistent with a mixture of low-Ca pyroxene, hematite, and Fe-bearing feldspar, whereas the lower Máaz formation members exhibit spectra characterized by broad absorption bands centered beyond 1000 nm, consistent with a mixture of high-Ca pyroxene and Fe-bearing feldspar (Horgan et al., 2022; Rice et al., 2022a). Exposures in the Guillaumes (Roubion member) and Bellegarde (Rochette member) abrasion patches analyzed with PIXL and SuperCam are consistent with a mineralogy dominated by laths of plagioclase and interlocking pyroxene (Schmidt et al., 2022; Udry et al., this issue). Farley et al. (2022) and Schmidt et al. (2022) classified Guillaumes and Bellegarde as micro-gabbros emplaced as lava flows. The geochemical trend observed across the diverse Máaz rocks shows an overall increase in silica and alkali elements upsection (Wiens et al., 2022). The lower Máaz member targets have mean abundances (standard deviation in parentheses) of SiO_2 of 45.4 (2.42) wt. %, Al_2O_3 of 6.4 (1.1) wt. %, FeO_T of 21.2 (3.0) wt. %, and MgO 4.6 (1.0) wt. %, and upper Máaz targets presented by Udry et al. (this issue) as fine- and coarse-grained have mean abundances of SiO_2 of 51.8 (2.6) wt. %, Al_2O_3 of 8.9 (1.3) wt. %, FeO_T of 17.9 (3.8) wt. %, and MgO 2.3 (0.6) wt. % (Udry et al., this issue).

The lower Máaz formation rocks exposed along the Artuby ridge (the Rochette member) were the second sample target of the Mars 2020 mission (Simon et al., this issue; Simon et al., 2022; Sun et al., 2022;), and the first successfully cored set of samples.

3 Methods

The Mastcam-Z instrument on the *Perseverance* rover is comprised of a pair of variable focal length multispectral charge-coupled device cameras to document the rover's surroundings (Bell et al., 2021; Bell et al., 2022). The cameras have a lowest zoom setting with a focal length of 26 mm and a highest zoom setting with a focal length of 110 mm. Between these two lowest and highest zoom settings the pixel scale varies between ~540 μm and ~148 μm at 2 m distance, and ~27 cm and ~6.7 cm at 1 km distance. The cameras have a filter set that allows acquisition of 11-point narrow-band spectra between 442–1022 nm (Bell et al., 2021). Mastcam-Z relies on radiometric calibration targets (Kinch et al., 2020) for reflectance-calibration of images, following a pipeline that is based on pre-flight testing and in-flight validation (Hayes et al., 2021). The calibration targets are routinely imaged together with commanded multispectral image sequences, and both these activities are typically executed within ± 90 minutes of local noon.

Spectra are extracted from multispectral images by selecting specific regions of interest in images from which reflectance factor (R*) values are averaged (Bell et al., 2021). After this, values from each camera are scaled by a single scaling factor per camera to make values from the two cameras agree at their overlapping wavelength at 800 nm. The scaling factor for each camera is defined to set the value at 800 nm to the average between the independently-derived values for the two cameras. Error bars shown indicate the standard deviation of pixels within each region of interest. Variations in spectra derived from multispectral images taken by the Mastcam-Z cameras can be caused by compositional and/or mineralogical characteristics of investigated materials related to the presence of certain Fe^{2+}-bearing silicates, Fe^{3+}-bearing oxides or oxyhydroxides, and OH^-- or H_2O-bearing alteration minerals, but also from changes in

texture, surface relief, illumination and viewing conditions, or the presence of materials covering surfaces such as dust or coatings (Bell et al., 2021, 2022; Rice et al., 2022a).

SuperCam is also situated on the *Perseverance* rover's mast, and is used for imaging and for measuring rock chemistry and mineralogy (Maurice et al., 2021; Wiens et al., 2021). In this study, we report results of rock chemistry measurements using Laser Induced Breakdown Spectroscopy (LIBS) and imaging of rock textures using the Remote Micro Imager (RMI). The LIBS instrument collects plasma light induced by a pulsed 1064 nm laser that is analyzed between 245 and 853 nm. Elements are identified by different emission lines in the LIBS spectrum. To accompany the LIBS data obtained on target surfaces, SuperCam has 23 calibration targets that are routinely imaged (Cousin et al., 2022). To characterize the chemistry of targets reported below we followed the work-flow defined in Udry et al. (this issue), which means we used the major-element oxide composition (MOC) calibration (Anderson et al., 2021) that builds on a suite of 1198 laboratory spectra on a total of 334 reference samples. The first five LIBS shots are removed from calculations because we are interested in the rock composition, not the composition of surface dust. The RMI uses red, green, and blue (RGB) filters to deliver visible color images with a field of view of 19 mrad and an angular optical resolution of 80 μrad (Maurice et al., 2021; Wiens et al., 2021).

Layer thicknesses across the Artuby outcrop were measured using The Planetary Robotics 3D Viewer (PRo3D) software, which is an interactive 3D visualization tool that allows users to work with high-resolution 3D reconstructions of the rover's surroundings (Barnes et al., 2018).

4 The Artuby ridge

The Artuby ridge is ~900 m long, constitutes an apparent "boundary" between the Máaz- and Séítah formations, and exposes 2−3 m of SW dipping lower Máaz formation stratigraphy. The outcrop extends from the Artuby East section, with its southeastern-most exposure at the Séítah southeast "thumb", and extends northwest (Figs. 1,2). The best exposures of strata imaged by *Perseverance* are the ~120 m long Artuby East section, which includes "type locality" Artuby_116 (Figs. 2a,3a), and the ~300 m long Artuby West section (Figs. 2a,4). We first obtained Mastcam-Z images of the Artuby ridge traversing south from the OEB landing. In these images the Artuby ridge protrudes as a cliff characterized by interbedded recessive and resistant layers (Fig 2b-d). En route to Séítah, *Perseverance* first investigated the Mure outcrop on sol 168 (Fig. 2a), before encountering the Artuby member to the northwest of Mure.

At the base of Artuby ridge lies the inferred contact, or transition, between the Séítah and Máaz formations (Farley et al., 2022). The contact itself is obscured by regolith and/or slump material from Artuby ridge and has not been imaged with *Perseverance*.

4.1 The Artuby member

The Artuby member rocks overlie the Séítah formation at the Artuby ridge and are characterized by distinct, yet morphologically variable, layering (Fig. 3, 4). The individual layers/laminations are on the order of mm to dm thick, and appear distinct because of differences in resistance to weathering/erosion. These characteristics result in resistant layers that protrude from the ridge, interbedded with more recessive materials (Fig. 3a-g, Fig. 5a). Different portions of the Artuby_116 outcrop, where the Artuby member is ~2.5 m thick, are characterized by mean

layer thicknesses that vary distinctly between outcrop sections (Fig. 3c). In the outcrop section that immediately underlies the Rochette member, i.e., the highest stratigraphic portions of the Artuby member, the mean layer thickness is 7−11 mm (variation caused by measurements on mosaics and corresponding 3D meshes from two different rover positions). In the section that underlies this, which is characterized by the presence of more knobbly layers, the mean layer thickness is 64−74 mm (Figs. 3, 5; Table S2; Fig. S4).

The resistant layers of the Artuby member are often irregular, knobbly, in appearance, and display rounded weathering surfaces. As the knobs weather, they expose subtle layering (Fig. 3b). This layering is also evident at exposures where the knobbliness is strongly weathered, and the outcrop appears more recessive (Fig. 3b), for example at the Rimplas workspace (Fig. 3h). In some places, pits in the more massive materials appear to cause partings, resulting in a layered, or laminated appearance (Fig. 3b). Accompanying the knobbly layers in Artuby are thinner, planar layers (Fig. 3d). These are in some instances highly recessive compared to underlying and overlying strata (Fig. 5c), and in some instances more erosionally resistant than the more massive units. At the Grasse outcrop, we observe thin, erosionally resistant layers that frame the more massive, knobbly layers (Fig. 3d, 5d). Generally, over the Artuby outcrops, the lateral appearance of the strata is highly variable, which makes it difficult to follow one layer over tens of meters of distance (Fig. 3). We have observed instances where the knobbly layers of Artuby appear to have slumped, or flowed, down over underlying strata (Fig. 3f-g, 4c).

Throughout the Artuby outcrops the Artuby member layers have a coarse, granular surface texture (Fig. 5c,d), and sometimes a reddish or purple coating or varnish (see Garczynski et al., this issue; Garczynski et al., 2022). The abraded surface of the Artuby member rock (Montpezat; Fig. S2) at the Rimplas workspace displays a fine-grained rock with interlocking crystal texture. Variation between the natural surface and the abraded surface texture is thus likely an effect of surface weathering.

Elemental chemistry obtained by SuperCam LIBS of six Artuby member targets (see Table S1 for a full list of analyzed targets) is consistent with a mineralogy that is dominated by plagioclase and a combination of augite, pigeonite, and possible clino-ferrosilite (Udry et al., this issue; Udry et al., 2022), with minor Fe-Ti-oxides, and an overall basaltic major element chemical composition (see also Wiens et al., 2022). Udry et al. (this issue) reports that SuperCam has not detected olivine in any rock targets of the Artuby member (or any other Máaz formation targets). The chemical composition throughout the entire Artuby ridge section is fairly homogenous, with a mean SiO_2 of 44.1 wt.%, and a mean Mg# [molar 100×(MgO/(MgO+FeO)] of 37 for the SuperCam targets we included in our analysis (i.e., the 13 targets marked in pink in Fig. 6; see also Udry et al., this issue). The stratigraphically lowest targets of the Artuby member are those at the Rimplas workspace (Figs. 2c, 3h), and the composition is consistent with the rest of Artuby.

4.2 The Rochette member

At Artuby ridge, the Artuby member rocks are overlain by the competent caprock member Rochette. The boundary between the two is often not clear, so distinguishing between the two members where only limited sections of rock are exposed is not always straightforward. The Rochette member is 30−50 cm thick and has less granular, smoother surface texture than the Artuby member, thus appearing more competent, or “massive”. The unit displays internal

structure in the form of (sub)horizontal layering and is pitted (Figs. 4, S1). Layers are generally approximately 4−5 cm thick and planar when viewed in the Artuby ridge section. Sub-planar/contorted layers are apparent on top of the ridge in the Citadelle workspace area (Fig. S1). The unit is relatively resistant to erosion, compared to some of the layers of the underlying Artuby member rocks, resulting in the cliff-like appearance of the ridge seen in views from Séítah towards Artuby (Fig. 2d). Compared to the Artuby member, where the more massive layers produce rounded weathering faces, weathering of Rochette produces angular, blocky boulders. The Rochette member extends from Artuby ridge south-southeast, forming flat-lying fractured surfaces similar in appearance to the pavers observed near the OEB landing site, that belong to the Naat'áanii member of the Máaz formation. The Rochette member appears to also form the margin of Máaz west of the landing site, but the Artuby member is not observed near the landing site in either outcrop or radar soundings (Crumpler et al., this issue; Horgan et al., this issue).

A paired set of samples, the Montdenier and Montagnac cores, and companion abrasion patch Bellegarde, were obtained in the Citadelle area, sols 181−199 (Fig. S2) on a small boulder (~40 cm across) called Rochette (Fig. S1). This area exposes only the Artuby ridge caprock, the Rochette member, which on top of the ridge displays parallel fluting and prominent mm- to cm-scale pits. Given the ~10° tilt to the south of strata of the Artuby ridge, the Citadelle workspace rocks, including the sampled Rochette boulder, are slightly higher in stratigraphy than the caprocks seen in section along the Artuby ridge. Morphologically (and chemically, Fig. 6 and below), rocks seen on top of the Artuby ridge appear largely consistent with those in the Citadelle workspace. The primary differences are the more pronounced vugginess of rocks in the Citadelle workspace compared to the Rochette member along the Artuby ridge, which may not be a primary difference in the characteristics of the rocks, but a result of better images and/or wind abrasion on the top of the ridge.

The Bellegarde abrasion patch exposes a fine-grained igneous textured rock with Mastcam-Z spectral signatures consistent with, for brown areas, a mixture of low-Ca pyroxene and hematite, and, for gray areas, high-Ca pyroxene (Horgan et al., 2022; Horgan et al., this issue). These occur together with plagioclase and minor Fe-Ti-oxides (Schmidt et al., 2022; Udry et al., this issue). Plagioclase and pyroxene crystals are 0.2−0.5 mm across (Schmidt et al., 2022; Simon et al., this issue), which is consistent with an aphanitic texture. Chemically, the Bellegarde abrasion patch is placed in the basalt compositional field (Simon et al., this issue; Udry et al., this issue).

4.3 Spectral properties and endmembers of Artuby ridge strata

We define the following spectral endmembers of Artuby ridge: dust, purple coatings, Artuby member thin layers (i.e., granular, (sub-)planar layers; top of Fig. 3e), Artuby member thick layers (generally knobblier layers of Artuby; Fig. 3f) plus Rochette member, and local regolith (Fig. 7). Based on the features of targeted areas in Mastcam-Z images (such as presence of coatings, thick dust, analyses of borehole tailings, and “clean” bedrock), we have added circles on Fig. 7a to show how the spectrally distinguishable endmembers plot (see Table S1 for a complete list of targets included in analysis). The thick layers of the Artuby member are largely spectrally (and chemically; Fig. 6; Udry et al., this issue; Udry et al., 2022) indistinguishable from the Rochette member on natural surfaces. These both exhibit Mastcam-Z spectra that vary from broad absorption centered beyond 900 nm, consistent with the presence of clinopyroxene,

to flat profiles >600 nm (Fig. 7b; see also Horgan et al., 2022; Rice et al., 2022a). No significant spectral indication of olivine has been detected in these rocks (or any other endmembers of the Artuby ridge) with Mastcam-Z, consistent with observations made by SuperCam LIBS (Udry et al., this issue; Udry et al., 2022). The abraded patches, Bellegarde (Rochette member) and Montpezat (Artuby member), are broadly similar spectrally, with one notable exception—it is possible to extract pyroxene spectra from the Bellegarde data, but not from Montpezat. Horgan et al. (2022) attributes this to differences in grain size between the two members.

The thin layers in Artuby exhibit Mastcam-Z spectra with a strong red slope <750 nm and a weak ~900 nm band (Fig. 7b). We also identify a 1030 nm downturn in the spectra (Rice et al., 2022a). The absorption band is consistent with a similar pyroxene mineralogy as the thick layers, but the strong red slope at short wavelengths suggests more ferric iron, and the downturn 1030 nm sometimes indicates hydration. Thus, the thin layers are likely of similar mineralogy as the thick layers but perhaps with some additional alteration and/or oxidation.

Both coatings and dust on rock surfaces can be resolved from bedrock in NIR spectra based on their strong ferric signatures (Fig. 7). Dust is spectrally characterized by flat spectra >750 nm and a strong red slope <750 nm, consistent with nanophase ferric oxides (Fig. 7b; Morris et al., 1993). Coatings exhibit Mastcam-Z spectra with a weak ~900 nm band, moderate red slope <750 nm, and strong 525 nm band (Fig. 7b; see Garczynski et al., this issue; Garczynski et al., 2022). The local regolith observed near the Artuby ridge is spectrally characterized by a broad strong band centered >900 nm, with a strong red slope <750 nm (Fig. 7b).

5 Discussion

The varied nature of the outcrop of Máaz rocks exposed along Artuby ridge tells a story of geologic evolution, be it evolution in the paleoenvironment such as a transition from subaerial igneous deposition to aqueous clastic deposition, or magmatic evolution with long-lived igneous activity with transitions in magma/eruption characteristics. Analysis of rock texture and morphology are crucial tools for determination of rock origin on Mars. Additionally, while we have many natural surface analyses of layers in Artuby ridge, we have only two abrasion patches where the abraded rock surface has been investigated. While the two abraded patches are likely basaltic lavas (Farley et al., 2022; Liu et al., 2022; Schmidt et al., 2022; Sun et al., 2022), the limited number is not representative of the variety of textures and morphologies observed across the Artuby ridge. Thus, further analysis is required to learn about the nature of the rocks that constitute the strata.

5.1 Artuby Ridge characteristics

The Artuby ridge displays a rich diversity in texture and morphology of rocks that are basaltic in composition (Udry et al., this issue). The outcrop is characterized by the presence of relatively erosionally resistant, knobbly, layers visible in Mastcam-Z images. The knobbly layers occur together with planar layers that have varied resistance to erosion, all appearing rough/granular in surface texture. The uppermost portion of the Artuby member exhibits finer-scale layering/lamination. The overlying Rochette member weathers differently, producing sharp-edged resistant blocks rather than the knobbly, rounded, faces of the more resistant layers

in the Artuby member. The morphological differences between the Artuby and Rochette members are not accompanied by clear differences in the spectral data or chemical data derived from analysis by SuperCam LIBS (Figs. 6, 7). In fact, throughout the entire Máaz formation, the mineral assemblage is uniform (plagioclase, augite, pigeonite, and possibly clino-ferrosilite), and minor variations in abundances and grain size over members/units lead to the different spectral shapes (Horgan et al., this issue). It is possible that some of the spectral differences between Artuby/Rochette and upper Máaz are caused by more high-Ca pyroxene. On Earth, olivine is an important constituent of basaltic rocks (Basaltic Volcanism Study Project, 1981), yet, as we have reported, neither Mastcam-Z nor SuperCam have detected olivine in Artuby ridge rocks. This does not mean that there is no olivine in these rocks, but rather that there is no significant amounts of coarse-grained olivine that can be resolved by these instruments. In fact, PIXL detected fayalitic olivine with secondary serpentine in the Guillaumes (Roubion member) and Bellegarde (Rochette member) abrasion patches (Schmidt et al., 2022), despite the rocks' normative normative mineralogy not including olivine. The lack of olivine, according to the Mastcam-Z and SuperCam investigation, is consistent with the interpretation that the rocks are Fe-rich basalts (Schmidt et al., 2022; Wiens et al., 2022) but we do not exclude the possibility that the rocks contain olivine, either in small amounts, of small grain size, or perhaps in altered form.

The thicker, resistant layers and knobs in Artuby spectrally resemble Rochette (Fig. 7), although the Artuby targets are often characterized by an overall redder color. This could be due to higher presence of ferric iron in the Artuby member than the Rochette member (e.g., Rice et al., 2022a). Because of difficulties in isolating spectra from the thinnest and most recessive layers in Artuby due to mantling by dust/regolith and the presence of coatings, we are not able to conclude whether the distinct spectral profile of some of these layers is in fact related to compositional/mineralogical differences, or whether the surface is causing the differences. What we can say, however, is that the Artuby and Rochette members are both distinct from the Bastide member of Séítah based on the absence of an olivine signature and the lower MgO content (Núñez et al., 2022; Udry et al., this issue; Udry et al., 2022; Wiens et al., 2022). Targets within the Séítah formation (excluding the Content member) have a mean of 23.5 wt.% MgO, compared to 2.3–4.6 wt.% MgO for Máaz formation targets (Udry et al., this issue; compare also results shown here in Fig. 6). On the other hand, the similarities in chemistry between the Content member, which overlies Bastide within the Séítah region (Fig. 1d), and Máaz formation rocks (specifically upper Máaz) are so pronounced that Udry et al. (this issue) suggest the two belong to the same petrogenetic sequence. The Content member is characterized by vesicular textures that Udry et al. (this issue) interpret to have formed by effusive volcanism, providing further separation from the rest of Séítah, since the other Séítah formation members are interpreted to represent an olivine cumulate (Farley et al., 2022; Liu et al., 2022). The targets within the Content member show very similar major element compositions to Máaz rocks (Udry et al., this issue), and the mineralogy is also similar in Content and Máaz, particularly for pyroxene compositions (Udry et al., this issue), although the Content member is somewhat more alkaline. The exact stratigraphic relation between the Content member and Máaz is however not clear from field observations with *Perseverance* (Fig. 1).

In turn, Rochette can be separated spectrally from the stratigraphically higher Máaz rocks, where Rochette rocks exhibit less absorption at short wavelengths, and overall bluer slopes (see also Horgan et al., 2022; Rice et al., 2022a). Compositionally, both the Artuby and Rochette members are more primitive than upper Máaz (Wiens et al., 2022; Udry et al., this

issue). Differences in chemistry of the regolith further highlights the variances in rock composition between on one side the Artuby and Rochette members, and on the other the stratigraphically higher Máaz rocks exposed near the OEB landing. We see that the regolith near Artuby, which is likely sourced from weathering of local bedrock, is spectrally distinct from typical regolith at the OEB landing (Fig. S3; see also Cardarelli et al., 2022; Vaughan et al., this issue).

5.2 Extrusive igneous emplacement

Earth analog sites are essential complements to robotic missions such as Mars 2020 to develop understanding of the geologic evolution of Mars (e.g., Farr, 2004; Osinski et al., 2006). In this contribution, we do not aim to describe any site on Earth as identical to what we see along the Artuby ridge, and do not attempt to present new Mars analog sites on Earth. Instead, we want to use the varied morphological characteristics of diverse well-described geologic deposits on Earth to understand similar characteristics on Mars, and to test hypotheses of martian geologic processes.

Earth offers us a wide range of analogs for planetary lava flow features. Even restricting our attention to mafic flows, we can observe a range of lava emplacement styles that depend upon effusion rate and the complexities of lava rheology. Changes in the nature of the eruption and evolution of the source magma over the period that the volcanics are being emplaced, as well as change with distance from the source, result in diverse lava flow morphologies (e.g., Self et al., 2021; Sheth, 2006; Voigt et al., 2021) that vary both laterally and vertically over a stratigraphic sequence (Fig. 8). Deposits of alternating pyroclastics and lava flows are common on Earth, resulting in even more complex morphological variations over a stratigraphic sequence than deposits formed by a single volcanic depositional mechanism (Fig. 8b). These types of alternating deposits in the same stratigraphic section, due to their intrinsic characteristics, have different resistance to weathering, resulting in recessive and resistant materials in the same section (Fig. 8b). We find that these features of terrestrial volcanic deposits have many commonalities with the strata at Artuby ridge, where we observe complex, varied morphologies that include repetition of sequences of units that share characteristics.

On Earth, flood basalt lobe thicknesses are generally >5 m (Self et al., 2021), with thinner lobes associated with basaltic shield volcanism, such as on Hawai‘i. The Artuby member is ~2–2.5 m thick at the Artuby ridge (Figs. 3,5), and composed of a series of layers with varying thicknesses between <1 to ~20 cm. The Rochette member appears ~2 m thick in radar soundings along the ridge (Horgan et al., this issue). Similary, nearer to the OEB landing site The Radar Imager for Mars Subsurface Experiment (RIMFAX) profiles shows a ~2 m thick unit with strong upper surface reflectors interpreted as the Rochette member (the Artuby member is not apparent in this area; Horgan et al., this issue).

For low-viscosity, basaltic compositions, low lava effusion rates (less than ~5–10 $m^3\ s^{-1}$ for Hawaiian tholeiite) typically lead to emplacement of compound, inflated pāhoehoe flow fields (Rowland and Walker, 1990), in which dominant feeder pathways (i.e., lava tubes or more laterally-extensive lava sheets) supply lava to the flow front beneath a solidifed, insulating surface crust. On shallow slopes, flows spread laterally, and continued injection under, and thickening of, the lava crust leads to vertical uplift (“inflation”) of the flow surface (Hon et al., 1994). Cooling and stalling at the flow front, or blockages within tubes/sheets, lead to breakouts of new flow lobes at quasi-random locations within the flow field. Thus, the flow field is

constructed from numerous overlapping, interfingering toes and lobes emplaced in a piecemeal manner in space and time. Initial flow lobes are dm to m-scale, but can thicken and inflate to several m over time (Hon et al., 1994). Cross sections through successions of pāhoehoe lobes exhibit highly variable morphologies on a range of scales, with simple lobes and toes showing a variety of features: lack of lateral continuity or uniformity, multiple overlapping lens-shaped or bulbous lobes, vertical or concentric cooling-related lamination within lobes, and smooth, ropey, or platey surface textures. At the Artuby scarp, lack of lateral continuity and undulating partings or contacts in some portions of the Rochette and Artuby members is consistent with multiple overlapping lobes, typically observed on dm- to m-scales (Fig. 3f-g, 4c, compare also knobbly, granular parts of Artuby in Fig. 3b with flow foliation in Fig. 8f). Bulbous morphologies ("knobbliness") similar to those we have observed in the Artuby member are also observed in terrestrial lava sections, either as a weathering expression or as a primary feature of pāhoehoe toes (Figs. 8b,f, 9a).

Higher effusion rates (greater than ~10 m^3 s^{-1} in Hawai'i; Rowland & Walker, 1990) typically produce channel-fed 'a'ā flows ranging up to the order of 10 m thick, characterized by rough clinkery surface and basal layers, with dense flow cores. These produce relatively simple lobate planforms, in contrast to the more complex compound form of pāhoehoe flow fields. In cross-section, the clinker layers of 'a'ā flows can preferentially weather out to form recessive layers. At the Artuby scarp, the capping Rochette member appears more laterally uniform than the Artuby layers, and the blocky pattern of jointing and fracturing is consistent with thicker terrestrial flows (Fig. 9b).

Vesicularity within successions of pāhoehoe lobes can be highly variable, given the range of morphologies and textures observed in terrestrial pāhoehoe examples (Fig. 9a–d). Vertical or concentric patterns of variability in vesicularity can be induced by the interplay of cooling (i.e., thermal and hence rheological gradients) and shearing within a flow lobe. Larger (> m scale) inflated flow sections typically exhibit vesicularity patterns in which a dense, low vesicularity core is sandwiched between upper and lower chilled zones. The upper portion of lava flows are frequently characterized by vertical gradations in vesicle size in which smaller, densely packed vesicles occur near the upper section and larger, but fewer, vesicles occur lower in the section, reflecting buoyant bubble rise and coalescence as the overlying crust continues to thicken (Fig. 8a). The upper portion of the Rochette member exhibits examples of vesicle size increasing with height, as might be the case beneath a chilled, more finely-vesicular surface crust (such as in Fig. 8a). Alignments of coarse vesicles (vesicle "trains") can be produced by trapping of buoyant bubbles beneath cooler, viscoelastic lava or solidified crust. The absolute vesicularity or gas volume per unit lava volume is controlled by the ideal gas law (Cashman & Kauahikaua, 1997) whereas vesicle sizes are controlled by coalescence according to the time available for growth before the downward and upward-moving solidification fronts set in. Similar patterns of vesicularity are observed to be suppressed in typical 'a'ā lava flows in which the interiors are relatively massive and vesicles are sparse (Figs. 8b, d). Weathering of especially vesicular zones can leave the dense portions protruding beyond the recessive weathered vesicular zones.

Development of paleosols or deposition of pyroclastic fall layers deposited between flows can produce prominent partings, as can internal shearing and continued injection of lava beneath cooling crusts, particularly in basal sections of lava flows. Complex layering or foliation can develop in this manner within lava flows over a range of viscosities in both pāhoehoe and 'a'ā sections from shearing strains during the late stages of flow (Fig. 8c–f). Finer laminations (such as we observe in Artuby scarp strata) within individual lobes may result from such

shearing and lead to vertical gradients or contrasts in rheology, vesicularity, and/or crystallinity of the lava. The recessive layers that we have observed can be produced by preferential weathering of more vesicular lava; differential aeolian erosion of the fine (cm-scale) vertical variability in vesicularity could potentially lead to the fine-scale laminations observed in the Rochette member (Fig. 4b-d).

Given that Jezero crater once hosted a lake, it is important to consider textures of subaqueously emplaced lavas. Lavas emplaced in water produce a range of morphologies, including pillows, lobes, and tubes (Skilling, 2002). Quench shattering of rapidly cooled lava skin and explosive magma–water interactions can occur to produce abundant glassy clastic material and accompanying granular textures. We do not observe features such as obvious pillow lavas or pillow breccias within the Artuby member. The mix of intact and fragmented lava morphologies with tephra and hyaloclastite can produce complex, rather disorderly sequences (White et al., 2015), but may include layered beds of clastic material.

Pyroclastic density current (PDC) deposits (Dufek et al., 2015) might exhibit a wide range of facies, depending on the PDC formation mechanism, current volume, particle concentration (dense vs. dilute), and evolution with distance from source. Deposits might exhibit massive to planar- or cross-bedded interior structures, complex interior stratigraphy, poor sorting, reverse grading, and welding. PDC deposits by nature tend to thicken in topographic lows, and thin over topographic highs. Fall deposits, on the other hand, tend to mantle topography more evenly, are better sorted than PDC deposits, and, depending on the relative steadiness of the eruptive source, may produce massive to planar-bedded deposits and grading. These are expected to contain significant amounts of glass (e.g., Houghton & Carey, 2015). The granular/clastic texture that we observe in at least some of the layers in the Artuby member (Fig. 5c) could be consistent with being a product of explosive volcanism, but we see no definitively diagnostic features of either pyroclastic fall or PDC deposits. Fall deposits could be consistent with the laterally continuous, planar layers of the Artuby member, which also tend to be more recessive. Furthermore, both fall deposits and hyaloclastites are typically associated with high abundances of glass. Glass has not been detected with SuperCam, although glass presence was inferred by Udry et al. (this issue) based on the presence of flow-banded textures, conchoidal fractures, and shiny luster observed on some rock targets (although wind polishing could also result in glassy-like appearance). Although the thinner planar layers were difficult to isolate in multispectral images, the slight spectral differences observed could be caused by alteration, which would be expected of more glassy layers.

5.3 Aqueous deposition

When first observing the fine-scale foliation, including sub cm-scale, in Artuby ridge in Mastcam-Z images, a sedimentary origin came to mind since fine-scale laminations are characteristic of deposition of clastic sediments in aqueous environments (see also Sun et al., this issue). Such laminations can typically be tied to a clastic sedimentary origin based on the presence of other accompanying morphological characteristics, such as cross-laminations. We have observed no unequivocally cross-laminated layers in the Artuby ridge. We have also not observed any other evidence of clastic sedimentary deposition, such as grain rounding, or presence of cement in the abrasion patches in the Rochette or Artuby members (see also discussion in Farley et al., 2022).

570 The well-developed state of the western delta in Jezero crater indicates that clastic
571 sediment input was significant, which also means that lacustrine sediments would have been
572 deposited in the lake. The depth of the Jezero crater lake is estimated to have been approximately
573 40 m based on the bottomset-foreset relationship in the western delta (Mangold et al., 2021). The
574 lacustrine sediments were deposited on top of the Máaz formation, if the delta does in fact post-
575 date these rocks (e.g., Holm-Alwmark et al., 2021; Stack et al., 2020). This means that the lack
576 of observed sedimentary rocks in Jezero crater thus far (the Séítah formation is also interpreted
577 as igneous rock; e.g., Farley et al., 2022; Liu et al., 2022; Núñez et al., 2022; Wiens et al., 2022)
578 opens up the question—where are the lake sediments?
579 Thus, erosion must have removed the entire lacustrine sedimentary record in Jezero
580 crater, at least from the most recent lake episode, that formed the western delta (see discussion in
581 Quantin-Nataf et al., 2021, this issue). The only exception is isolated mesas of deltaic/lacustrine
582 deposits (e.g., Holm-Alwmark et al., 2021; Mangold et al., 2021). If parts of the lacustrine phase
583 in Jezero crater that is tied to formation of the western delta pre-dates deposition of (parts of) the
584 Máaz formation, then lacustrine sedimentary rocks can be preserved either in the Máaz formation
585 rock sequence, or in a stratigraphically lower position. Lacustrine phases in Jezero crater that
586 pre-date the phase of formation of the western delta are supported by the presence of the much
587 less well-preserved northern fan with a possibly separate inflow channel (e.g., Jodhpurkar &
588 Bell, 2021). No direct evidence of clastic sediment deposition was observed in situ in the lower
589 Máaz formation by us, or by Horgan et al. (2022; this issue) and Udry et al. (this issue) did not
590 observe any such lithologies in the upper Máaz members either. However, RIMFAX soundings
591 show that it is possible that Rochette is overlain by a localized ~1 m thick low-density
592 sedimentary unit at least in places along the western margin of Máaz in the landing site area
593 (Horgan et al., this issue), meaning that preserved clastic sediments could be present both
594 stratigraphically lower than lavas of the Máaz formation, and in higher stratigraphic positions
595 than Artuby/Rochette within the Máaz formation.
596

597 5.4 Intrusive igneous emplacement

598 On Earth, olivine cumulates are part of a petrogenetic sequence of rocks that also usually
599 contain overlying ferrogabbros, or pyroxene-rich cumulates (e.g., Namur et al., 2015). Farley et
600 al. (2022) and Liu et al. (2022) propose that the Séítah formation is an olivine cumulate, and that
601 the lower Máaz rocks may be petrogenetically related (see also Sun et al., this issue; Wiens et al.,
602 2022). Thus, evaluating the potential origin of Artuby ridge strata as part of the same
603 petrogenetic sequence is necessary. We evaluate the potential of the foliation observed in lower
604 Máaz to have been formed in an igneous intrusion first. Layered structures and banding of
605 intrusive igneous bodies on Earth can be highly variable (Davies et al., 1980; Hirschmann, 1992;
606 Hoover, 1989; McBirney, 1996; Namur et al., 2010, 2015), such as in the Skaergaard intrusion,
607 and in the Sept Iles layered intrusion, where individual recognizable layers range from ~10 cm to
608 > 1 m. Thinner, cm-scale, beds occur in for example the Stillwater Complex (McCallum, 1996),
609 and sub-cm scale beds, are known for example from the La Cordadera gabbro intrusion in Chile
610 (Namur et al., 2015). These would be a closer analog to the scale of bedding/lamination that we
611 observe in Artuby ridge. However, we are not aware of any terrestrial layered igneous intrusion
612 that display such flow-like structures as observed in the Artuby ridge, or form lobate margins
613 such as observed within the Máaz formation rocks exposed at the Artuby scarp. We also note
614 that the pitted texture of the Rochette member may be difficult to reconcile with a petrogenetic

relationship with the cumulate rock in Séítah. The mineralogy of Rochette/Artuby is also inconsistent with an origin from the same magma source as Séítah, as the pyroxene suites are of very different compositions (Udry et al., this issue).

5.5 Summary of the origin of Artuby ridge strata

The knobbly layers and the Rochette member of the Artuby ridge share many morphological characteristics with lava flows on Earth, such as the complex lobe/intraflow textures and presence of vesicles (compare Figs. 3f,g with 8b and 9 a,b, and d). We also note similarities in variable friability that in our Hawai‘i example are due to the presence of a somewhat weathered ‘a‘ā clinker. The textures and morphologies of the Artuby and Rochette members at Artuby ridge are thus consistent with interior structures of terrestrial mafic lava flows having a range of emplacement styles and weathering expressions (Fig. 5). Our conclusion is further supported by the spectral character and chemical composition, as well as textures observed in the abraded patches in both Artuby and Rochette, which lack evidence for typical clastic sedimentary rocks such as roundedness of grains and presence of cement.

Taken together, the morphology and compositional data of the more massive layers in Artuby (i.e., the knobbly layers and Rochette member), provide convincing evidence that these units are effusive in origin. Along the Artuby ridge, the Artuby and Rochette members range up to 2–2.5 and 2 m thick, respectively. While we can infer the thickness of both members from RIMFAX data (Horgan et al., this issue) without seeing the lower portion of Artuby due to regolith cover, these are likely underestimates of the true thickness of the members because the upper portion of Rochette may have been eroded (Quantin-Nataf et al., 2021, this issue). Likewise, the Artuby member may have been eroded before emplacement of Rochette, and may include erosional surfaces. In addition, each member may be composed of multiple, thinner flow lobes. Typical basaltic shield flows are on the order of dm to a few m; flood basalts can be substantially thicker. Nevertheless, the small thicknesses of Artuby and Rochette might be suggestive of thin, low-viscosity flow units and/or the distal lobes of compound flow fields.

The rough, somewhat granular surface texture of Artuby member rocks could be the result of the breakdown of finely vesicular lava and resembles the foliated interior shown in Fig. 8f. The finely-layered, planar material that appears to be intercalated or to surround the bulbous Artuby member morphologies (Fig. 3d) is difficult to explain by an effusive origin. These seem to be broadly consistent in composition to the rest of the Artuby and Rochette member targets, which agrees with a scenario where these layers are derived from the same source as the more massive layers, albeit via a different mechanism (e.g., tephra deposits). They could also be weathered ‘a‘ā clinker layers, or even hyaloclastites produced in the presence of external water. It is also possible that the Artuby ridge contains layers of material deposited via aeolian processes during periods of time when volcanic products were not emplaced.

It is likely that the Artuby ridge section exposes material that experienced weathering for various durations, and development of regolith could give rise to the variable morphologies and resistance to weathering that we observe. This is also consistent with the similarities in chemistry and spectral properties across the rock members. More pronounced weathering of some sections of knobbly materials could also give rise to more layered than knobbly appearance, since the knobbly material appears to have an internal foliation (Figs. 3b, h).

659 ### 5.6 Implications for the Séítah/Máaz relationship

660 The Artuby ridge exposes the stratigraphically lowest Máaz formation rocks, the Artuby
661 and Rochette members. These members overlie the Séítah formation, which occurs outside of the
662 lobate margins of Máaz (Fig. 1b; see also Hamran et al., 2022). However, with the contact
663 obscured, a genetic relationship has not been tested directly during the Mars 2020 crater floor
664 exploration campaign.
665 Orbital mapping along the Máaz–Séítah contact farther to the south in Jezero crater
666 revealed discrete layers in the basal 2–6 m of the Máaz formation (exposed both outside and
667 inside of the lobate margins), which change in overall thickness and in the number of observed
668 layers (Alwmark et al., 2021). Alwmark et al. (2021) suggested that these observations indicate
669 that layered strata were likely deposited over existing topographic relief associated with an
670 erosional unconformity between the units. Based on our results, it is possible that these variations
671 in both thickness and in the number of observed layers from orbit could result (at least partly)
672 from lobe geometry rather than an erosional unconformity between the formations. In situ
673 analysis with RIMFAX on *Perseverance* has shown that layers at the Séítah and Máaz contact
674 are tilted at the same angle (Farley et al., 2022). This was used to argue in Farley et al. (2022)
675 that both formations were tilted at the same time, potentially indicating that the formations were
676 deposited relatively close in time.
677 While Máaz and Séítah share some morphological characteristics, such as interlayering of
678 thin beds and lateral transitions from recessive to resistant behavior, they are chemically and
679 mineralogically distinct (Rice et al., 2022a; Sun et al., 2022; Udry et al., this issue; Udry et al.,
680 2022; Wiens et al., 2022). The one exception is the Content member, representing the highest
681 stratigraphic targets analyzed within the Séítah region, which is distinct from the rest of Séítah
682 and has both textural and chemical/mineralogical similarities with the Máaz formation (Udry et
683 al., this issue). Additionally, whereas Máaz has clear boundaries that define the extent of the
684 formation, Séítah does not, although the exact geographic limits and extents of the different
685 Máaz members is somewhat unclear at this time.
686 Olivine cumulates have been described in settings of layered mafic intrusions, thick lava
687 flows/ponds, shallow sills/laccoliths, or in impact melt sheets (e.g., Brown et al., 2004). In
688 terrestrial examples olivine cumulates are known to occur stratigraphically below pyroxene-rich
689 igneous rocks, as part of the same sequence. In these rocks the overall chemical trend of the
690 minerals increase in Fe, Na, and K upwards in stratigraphy. The chemical composition of the
691 overlying Máaz formation rocks may thus at first hand appear to be the natural follow-on of that
692 same petrogenetic sequence. However, our conclusion that Artuby ridge rocks represent lavas
693 with potential intercalated tephra deposits and weathering products, is not consistent with a
694 scenario where lower Máaz is part of the same petrogenetic sequence as Séítah. Analysis of
695 SuperCam data further supports our observations that it is unlikely that the Artuby ridge rocks
696 represent the same petrographic sequence as Séítah. Udry et al. (this issue) exclude the same
697 parental magma for the Séítah and Máaz formations based on the chemical composition and
698 mineralogy of the rocks. An extended period of erosion would thus be necessary to remove the
699 upper portion of the Séítah cumulate (the portion poor in olivine) since the Artuby ridge rocks
700 are not compatible with a scenario where those rocks represent that upper cumulate portion,
701 indicating that some time passed between emplacement of the Séítah and Máaz formations (see
702 also discussion in Horgan et al., this issue).
703

5.7 Implications for regional geology and Mars sample return

The Máaz formation has been proposed to be related to the capping unit mapped outside of Jezero crater, the Circum-Isidis regional capping unit (e.g., Bramble et al., 2017; Hundal et al., 2022). The age of this unit is likely somewhere between 3.6 and 3.96 Ga, constrained by the formation of the Isidis basin (Werner, 2008) and Syrtis Major lavas (Mustard et al., 2009). A lava flow is not a viable explanation as an emplacement mechanism for the whole capping unit because it spans too large a range in elevation (see also discussion in Sun & Stack 2020a,b), and because exposures of the unit tend to drape topography (Hundal et al., 2022). Hundal et al. (2022) favors a pyroclastic depositional scenario for the capping unit because it thinly drapes topography, including depressions, it is regionally uniform, has m-scale bands of variable tonality, and additionally because of the stratigraphic and geomorphic similarities to the regional olivine-rich unit that is proposed to be an ashfall deposit (Kremer et al., 2019; Mandon et al., 2020). The capping unit is always found overlying the olivine-rich unit, suggesting a shared origin (Hundal et al., 2022).

A pyroclastic depositional scenario for the regional unit is, however, inconsistent with the scenario proposed here for lower Máaz, where the majority of the Máaz formation in the Artuby ridge is lava, and also with upper Máaz, which is also interpreted to be lava (e.g., Crumpler et al., this issue; Horgan et al., 2022; Horgan et al., this issue). Our results thus indicate that either Máaz is not related to the regional capping unit, or the unit mapped as the regional capping unit itself consists of a number of individual geologic deposits with similar orbital morphological and spectral properties, that are not necessarily related. The Rochette member has also been mapped along the borders of Séítah further north of the Artuby ridge (Crumpler et al., this issue), was emplaced as lava flow(s) embaying Séítah, and is thus likely the unit (perhaps together with the Artuby member) that is forming the lobate margins of the "Jezero crater dark-toned floor" throughout Jezero crater (Horgan et al., this issue). The upper Máaz formation, on the other hand, seems to have a more limited spatial occurrence in Jezero crater (Horgan et al., this issue), and was not identified as separate from the unit causing the lobate margins in earlier orbital investigations (e.g., Goudge et al., 2015; Hundal et al., 2022; Stack et al., 2020). Because of the presence of potential erosional surfaces between lower and upper Máaz, and within both upper Máaz (Horgan et al., this issue) and lower Máaz, there may be significant time periods separating emplacement of lower Máaz and upper Máaz, despite the similar chemistries. This could mean that individual exposures of the regional capping unit, despite similar chemistry (i.e., spectral signature), may also have been deposited with significant time gaps.

Alternatively, the individual geologic deposits that constitute the regional capping unit may be related but were formed by different emplacement processes, for example, both effusive and explosive phases from a given source. Or, in a different scenario, the capping unit could be comprised of deposits from multiple, compositionally similar sources with a range of eruption styles. Some of the regional outcropping units (including the Artuby formation) may have been emplaced as lava flows during a major regional volcanic episode, followed by emplacement of other units as pyroclastic fall, such as is indicated in the stratigraphy of Artuby ridge (Fig. 5). Then, more lava flows, including the Rochette member, were emplaced. Further comparison with the regional capping unit (and comparison between olivine-bearing units within and outside Jezero crater) will be possible as *Perseverance* continues to traverse up and beyond the western delta. Until then, the issue of the relationship between the Máaz formation and the regional capping unit remains an issue to be resolved.

A global shift in the character of Mars volcanism has been inferred to have happened in the Late Noachian/Early Hesperian (Bandfield et al., 2013; Baratoux et al., 2013; Mustard et al., 2005; Poulet et al., 2009; Robbins et al., 2011), both in terms of eruptive character (from generally explosive to generally effusive) and in dominant pyroxene mineralogy of the volcanic products (from low-Ca to high-Ca). Although the underlying cause for this is poorly understood, the observations made by *Perseverance* of the Jezero crater floor have important implications for the evolution and character of the martian mantle. We show that the nature of martian volcanic activity is complex and variable, at a resolution not discernable with orbital data, and that effusive volcanic products dominate the Artuby and Rochette members of the Máaz formation in Jezero crater, interbedded with products that are potentially compatible with explosive volcanism.

Thin flow lobes, such as those exposed in the Artuby ridge, differ from flood basalts on Earth, and may indicate relatively small eruptive fluxes (Self et al., 2021). Thin flow lobes could also be an indication of being far from the source. Horgan et al. (2020) hypothesized that the source for lava flows in the crater could be fissures and dikes in the crater floor that are covered by the unit, or the conical and cratered edifice located on the southeastern rim of Jezero crater (Fig. 1). Ravanis et al. (2022) noted the presence of enigmatic conical features located in the marginal unit adjacent to the crater rim inside the crater, and Horgan et al. (this issue) reported on a ~200 m high isolated edifice located just inside the northern crater rim of Jezero. The presence of fine-scale layers near the top of the Artuby member could indicate a transition to more explosive eruptions, followed by a hiatus of deposition and then formation of the Rochette member as a lava flow. The superposition and similar chemistries of the two members argue in favor of the Artuby and Rochette members being derived from a single reservoir, yet their distinctly different morphologies—with Artuby having a rough, granular, texture that appears almost clastic, and Rochette being more massive with vesicles—indicate some change in the eruptive characteristics, perhaps through replenishment of the magma reservoir.

Mars Sample Return will provide a set of samples from the Jezero crater floor that when analyzed on Earth will yield unprecedented insight into martian magmatic evolution. However, these are limited in number compared to the complex set of layers and morphologies that we observe in the Artuby ridge, and alone cannot provide the whole picture of geologic evolution. Thus, establishing the geologic context is extremely important for both the interpretation of samples and for increasing our understanding of martian geologic evolution.

6 Conclusions

We have presented a geomorphologic analysis of Mastcam-Z images and multispectral information alongside chemical analysis by SuperCam compared with analog sites on Earth that we used to interpret the origins of rocks found along the Artuby Ridge, a ~900 m scarp on the floor of Jezero crater. There are two members of the Máaz formation exposed at the Artuby ridge: the Artuby member, which consists of morphologically distinct units, and the Rochette member, which overlies the Artuby member. Our analysis of the varied morphological expression of the rocks exposed shows that they are consistent with a primary igneous deposition as lava flows. This is due to the primary mineralogy, the basaltic major element composition, and the presence of interlocking grains in abrasion patches, vesicles and vesicle trains, jointed crystals, potential flow textures, variations between more massive, knobbly appearance, and layers of alternating thicknesses. There remain a number of textures which are difficult to

794 explain with an origin as purely lava flows, namely the presence of laterally continuous,
795 sometimes recessive, thin layers of alternating friability that "frame" more bulbous portions of
796 the Artuby member. We suggest that these thin layers may be the result of preferential
797 weathering of shear zones of high vesicularity layers within the lava, the interbedding of lava and
798 ash/tephra, weathered 'a'ā clinker layers, or aeolian deposition, or alternatively, that they may be
799 hyaloclastite developed in the presence of external water, although we do not see compelling
800 evidence of emplacement in water.
801 Our results show that either (1) the Máaz formation and the regional mafic capping unit
802 are unrelated, or (2) that the two are related, but were formed via different emplacement
803 mechanisms, to explain both the observations at Artuby ridge and the broad-scale characteristics
804 of the regional unit (e.g., its draping morphology).
805 Our analyses provide geologic context for the Máaz formation samples that, upon their
806 arrival to Earth, will be analyzed with high-end laboratory equipment available at that time. Our
807 results highlight the diversity of geologic units on Mars not visible from orbit.

808

809 **Acknowledgments**

810 The authors would like to thank the Mars 2020 science and engineering teams for their efforts in
811 running the mission and in collecting data, and for discussion. A special thanks is extended to
812 Mastcam-Z Payload Downlink Leads for regenerating mosaics for this contribution. Professional
813 editorial handling by L. Montési and thorough reviews by Christopher Hamilton and one
814 anonymous reviewer is gratefully acknowledged. S. Alwmark was supported by an International
815 Postdoc grant from the Swedish Research Council (grant # 2017-06388). A. Udry was supported
816 by a NASA grant (80NSSC21K0330). The participation of O. Gasnault in SuperCam on
817 *Perseverance* was supported by CNES. D. Flannery acknowledges funding by the Australian
818 Research Council. K. B. Kinch was supported by the Carlsberg Foundation grant CF19-0023. E.
819 Cloutis acknowledges funding from the Canadian Space Agency and the Natural Sciences and
820 Engineering Research Council of Canada. B. Horgan, J. Núñez, E. Ravanis, and S. Fagents were
821 funded by NASA's Mars 2020 Project via a subcontract from the California Institute of
822 Technology/Jet Propulsion Laboratory to Arizona State University (subcontract 1511125).
823

824 **Open Research**

825 The data in this publication are from the Mastcam-Z and SuperCam instruments onboard the
826 NASA Mars 2020 *Perseverance* rover. The SuperCam data are from LIBS and RMI. The data
827 are available through the Planetary Data System Imaging Node (https://pds-
828 imaging.jpl.nasa.gov/portal/mars2020_mission.html), and GeoSciences Node (https://pds-
829 geosciences.wustl.edu/missions/mars2020/). For Mastcam-Z data, see Bell & Maki (2021). The
830 Mastcam-Z multispectral database from sols 0–380 is published in Rice et al. (2022b). For
831 SuperCam data, see Wiens & Maurice (2021).
832
833

834 **References**

835 Alwmark, S., Kah, L., Garczynski, B., Scheller, E. L., Smith, R. J., Stack, K. M., et al. (2021)
836 Detailed orbital mapping highlights relationships among Jezero crater floor units. *Geological*
837 *Society of America Abstracts with Programs*, 53. doi:10.1130/abs/2021AM-369062
838
839 Anderson, R. B., Forni, O., Cousin, A., Wiens, R. C., Clegg, S. M., Frydenvang, J., et al. (2022).
840 Post-landing major element quantification using SuperCam laser induced breakdown
841 spectroscopy. *Spectrochimica Acta Part B: Atomic Spectroscopy*, 188, 106347.
842 doi:10.1016/j.sab.2021.106347
843
844 Bandfield, J. L., Edwards, C. S., Montgomery, D. R., & Brand, B. D. (2013). The dual nature of
845 the Martian crust: Young lavas and old clastic materials. *Icarus*, 222, 188–199.
846 doi:10.1016/j.icarus.2012.10.023
847
848 Baratoux, D., Toplis, M. J., Monnereau, M., & Sautter, V. (2013). The petrological expression of
849 early Mars volcanism. *Journal of Geophysical Research: Planets*, 118, 59–64.
850 doi:10.1029/2012JE004234
851
852 Barnes, R., Gupta, S., Traxler, C., Ortner, T., Bauer, A., Hesina, G., et al. (2018). Geological
853 Analysis of Martian Rover-Derived Digital Outcrop Models Using the 3-D Visualization Tool,
854 Planetary Robotics 3-D Viewer—PRo3D. *Earth and Space Science*, 5, 285–307.
855 doi:10.1002/2018EA000374
856

857 Basaltic Volcanism Study Project. (1981). *Basaltic Volcanism on the Terrestrial Planets*. New
858 York, USA: Pergamon Press, Inc.
859
860 Bell III, J. F., & Maki, J. M. (2021). Mars 2020 Mast Camera Zoom Bundle. NASA Planetary
861 Data System. doi:10.17189/1522843
862
863 Bell III, J. F., Maki, J. N., Mehall, G. L., Ravine, M. A., Caplinger, M. A., Bailey, Z. J., et al.
864 (2021). The Mars 2020 Perseverance rover Mast Camera Zoom (Mastcam-Z) multispectral,
865 stereoscopic imaging investigation. *Space Science Reviews*, 217, 24. doi:10.1007/s11214-020-
866 00755-x
867
868 Bell III, J. F., Maki, J. N., Alwmark, S., Ehlmann, B. L., Fagents, S. A., Grotzinger, J. P., et al.
869 (2022). Geological, multispectral, and meteorological imaging results from the Mars 2020
870 *Perseverance* rover in Jezero crater. *Science Advances*, 8, eabo4856.
871 doi:10.1126/sciadv.abo4856
872
873 Bramble, M. S., Mustard, J. F., & Salvatore, M. R. (2017). The geological history of Northeast
874 Syrtis Major, Mars. *Icarus*, 293, 66–93. doi:10.1016/j.icarus.2017.03.030
875
876 Brown, A., Walter, M., & Cudahy, T. (2004). Short-wave infrared reflectance investigation of
877 sites of paleobiological interest: Applications for Mars exploration. *Astrobiology*, 4.
878 doi:10.1089/ast.2004.4.359
879

880 Brown, A. J., Viviano, C. E., & Goudge, T. A. (2020). Olivine-carbonate mineralogy of the
881 Jezero crater region. *Journal of Geophysical Research: Planets*, 125, e2019JE006011.
882 doi:10.1029/2019JE006011
883
884 Cardarelli, E. M., Vaughan, A., Minitti, M. E., Beegle, L., Rice, M., Johnson, J. R., et al. (2022).
885 *Regolith at Jezero crater, Mars: Spectral diversity, textures, and implications for provenance.*
886 Paper presented at 53rd Lunar and Planetary Science Conference, The Woodlands, TX, Abstract
887 #2858.
888
889 Carr, M. (2018). *The surface of Mars*. Cambridge, UK: Cambridge University Press.
890
891 Cashman, K. V., & Kauahikaua, J. P. (1997). Reevaluation of vesicle distributions in basaltic
892 lava flows. *Geology*, 25, 419–422. doi:10.1130/0091-7613(1997)025<0419:ROVDIB>2.3.CO;2
893
894 Chapman, M. G. (2007). *The geology of Mars: Evidence from Earth-based analogs*. Cambridge,
895 UK: Cambridge University Press.
896
897 Cousin, A., Sautter, V., Fabre, C., Dromart, G., Montagnac., G., Drouet, C., et al. (2022).
898 SuperCam calibration targets on board the Perseverance rover: Fabrication and quantitative
899 characterization. *Spectrochimica Acta Part B: Atomic Spectroscopy*, 188, 106341.
900 doi:10.1016/j.sab.2021.106341
901

902 Crumpler, L., et al. (this issue). In Situ Geologic Context Mapping Transect on the Floor of
903 Jezero Crater from Mars 2020 Perseverance Rover Observations. This issue.
904
905 Davies, G., Cawthorn, R. G., Barton, J. M. & Morton, M. (1980). Parental magma to the
906 Bushveld Complex. *Nature*, 287, 33–35. doi:10.1038/287033a0
907
908 Dufek, J., Ongaro, T. E, Roche, O. (2015). Pyroclastic density currents: Processes and models. In
909 H. Sigurdsson, B. Houghton, S. McNutt, H. Rymer, & J. Stix (Eds.), *The Encyclopedia of*
910 *Volcanoes* (pp. 617–629). Academic Press.
911
912 Eales, H. V., & Cawthorn, R. G. (1996). The Bushveld Complex. In R. G. Cawthorn (Ed.)
913 *Layered Intrusions* (pp. 181–229). Amsterdam: Elsevier.
914
915 Ehlmann, B. L., Mustard, J. F., Fassett, C. I., Schon, S. C., Head, J. W. III, Des Marais, D. J., et
916 al. (2008). Clay minerals in delta deposits and organic preservation potential on Mars. *Nature*
917 *Geoscience*, 1, 355–358. doi:10.1038/ngeo207
918
919 Farley, K. A., Williford, K. M., Stack, K. M., Bhartia, R., Chen, A., de la Torre, M., et al. (2020).
920 Mars 2020 mission overview. *Space Science Reviews*, 216, 142. doi:10.1007/s11214-020-00762-
921 y
922

Farley, K., Stack, K. M., Shuster, D. L., Horgan, B. H. N., Hurowitz, J. A., Tarnas, J. D., et al. (2022) Aqueously altered igneous rocks sampled on the crater floor of Jezero crater, Mars. *Science*, 377, eabo2196. doi: 10.1126/science.abo2196

Farr, T. G. (2004). Terrestrial analogs to Mars: The NRC community decadal report. *Planetary and Space Science*, 52, 3–10. doi:10.1016/j.pss.2003.08.004

Fassett, C. I., & Head III, J. W. (2005). Fluvial sedimentary deposits on Mars: Ancient deltas in a crater lake in the Nili Fossae region. *Geophysical Research Letters*, 32, L14201. doi:10.1029/2005GL023456

Fassett, C. I., & Head III, J. W. (2008a). The timing of Martian valley network activity: Constraints from buffered crater counting. *Icarus*, 195, 61–89. doi:10.1016/j.icarus.2007.12.009

Fassett, C. I., & Head III, J. W. (2008b). Valley network-fed, open-basin lakes on Mars: Distribution and implications for Noachian surface and subsurface hydrology. *Icarus*, 198, 37–56. doi:10.1016/j.icarus.2008.06.016

Fergason, R. L., Galuszka, D. M., Hare, T. M., Mayer, D. P., & Redding, B. L. (2020). Mars 2020 terrain relative navigation HiRISE orthorectified image mosaic [data set]. U.S. Geological Survey. doi:10.5066/P9QJDP48

945 Garczynski, B. J., Bell III, J. F., Horgan, B. H. N., Johnson, J. R., Rice, M. R., Vaughan, A., et
946 al. (2022). *Perseverance and the purple coating: A Mastcam-Z multispectral story*. Paper
947 presented at 53rd Lunar and Planetary Science Conference, Houston, TX, Abstract #2346.
948
949 Garczynski, B. J., et al. (this issue). Evidence of alteration on the Jezero crater floor: A Mastcam-
950 Z multispectral analysis. This issue.
951
952 Garvin, J. B., Sakimoto, S. E. H., & Frawley, J. J. (2003). *Craters on Mars: Global geometric*
953 *properties from gridded MOLA topography*. Paper presented at Sixth Internation Conference on
954 Mars, Pasadena, CA, Abstract #3277.
955
956 Goudge, T. A., Head III, J. W., Mustard, J. F., & Fassett, C. I. (2012). An analysis of open-basin
957 Lake deposits on Mars: Evidence for the nature of associated lacustrine deposits and post-
958 lacustrine modification processes. *Icarus*, 219, 211–229. doi:10.1016/j.icarus.2012.02.027
959
960 Goudge, T. A., Mustard, J. F., Head III, J. W., Fassett, C. I., & Wiseman, S. M. (2015).
961 Assessing the mineralogy of the watershed and fan deposits of the Jezero crater paleolake
962 system, Mars. *Journal of Geophysical Research: Planets*, 120, 775–808.
963 doi:10.1002/2014JE004782
964
965 Goudge, T. A., Milliken, R. E., Head III, J. W., Mustard, J. F., & Fassett, C. I. (2017).
966 Sedimentological evidence for a deltaic origin of the western fan deposit in Jezero crater, Mars

967 and implications for future exploration. *Earth and Planetary Science Letters*, 458, 357–365.
968 doi:10.1016/j.epsl.2016.10.056
969
970 Hamran, S-E., Paige, D. A., Allwood, A., Amundsen, H. F., Berger, T., Brovoll, S., et al. (2022).
971 Ground penetrating radar observations of substructures in the floor of Jezero crater, Mars.
972 *Science Advances*, 8, eabp8564. doi: 10.1126/sciadv.abp8564
973
974 Hayes, A., Corlies, P., Tate, C., Barrington, M., Bell, J. F., Maki, J. N., et al. (2021) Pre-flight
975 calibration of the Mars 2020 rover Mastcam Zoom (Mastcam-Z) multispectral, stereoscopic
976 imager. *Space Science Reviews*, 217, 29. doi:10.1007/s11214-021-00795-x
977
978 Herd, C. D. K., Bosak, T., Stack, K. M., Sun, V. Z., Benison, K. C., Cohen, B. A., et al. (2021).
979 *Sampling Mars: Notional caches from Mars 2020 strategic planning*. Paper presented at 52nd
980 Lunar and Planetary Science Conference, The Woodlands, TX, Abstract #1987.
981
982 Hirschmann, M. M. (1992). Origin of the transgressive granophyres from the layered series of
983 the Skaergaard intrusion, East Greenland. *Journal of Volcanology and Geothermal Research,* 52,
984 185-207. doi:10.1016/0377-0273(92)90140-9
985
986 Holm-Alwmark, S., Kinch, K. M., Hansen, M. D., Shahrzad, S., Svennevig, K., Abbey, W. J., et
987 al. (2021). Stratigraphic relationships in Jezero crater, Mars: Constraints on the timing of fluvial-
988 lacustrine activity from orbital observations. *Journal of Geophysical Research: Planets*, 126,
989 e2021JE006840. doi:10.1029/2021JE006840

Hon, K., Kauahikaua, J., Denlinger, R., & Mackay, K. (1994). Emplacement and inflation of pahoehoe sheet flows: Observations and measurements of active lava flows on Kilauea Volcano, Hawaii. *Geological Society of America Bulletin*, 106, 351–370. doi: 10.1130/0016-7606(1994)106<0351:EAIOPS>2.3.CO;2

Hoover, J. D. (1989). The chilled marginal gabbro and other contact rocks of the Skaergaard intrusion. *Journal of Petrology,* 30, 441-476. doi:10.1093/petrology/30.2.441

Horgan, B. H. N., Anderson, R. B., Dromart, G., Amador, E. S., & Rice, M. S. (2020). The mineral diversity of Jezero crater: Evidence for possible lacustrine carbonates on Mars. *Icarus*, 339, 113526. doi:10.1016/j.icarus.2019.113526

Horgan, B., Rice, M., Garczynski, B., Johnson, J., Stack-Morgan, K., Vaughan, A., et al. (2022). *Mineralogy, morphology, and geochronological significance of the Máaz formation and the Jezero crater floor*. Paper presented at 53rd Lunar and Planetary Science Conference, The Woodlands, TX, Abstract #1680.

Horgan, B., Udry, A., Rice, M., Alwmark, S., Amundsen, H., Bell, J., et al. (this issue). Mineralogy, morphology, and emplacement history of the Maaz formation on the Jezero crater floor from orbital and rover observations.

1012 Houghton, B., & Carey, R. J. (2015) Pyroclastic fall deposits. In H. Sigurdsson, B. Houghton, S.
1013 McNutt, H. Rymer, & J. Stix (Eds.), *The Encyclopedia of Volcanoes* (pp. 599–616). Academic
1014 Press.
1015
1016 Hundal, C. B., Mustard, J. F., Kremer, C. H., Tarnas, J. D., & Pascuzzo, A. C. (2022). The
1017 Circum-Isidis Capping Unit: An Extensive Regional Ashfall Deposit Exposed in Jezero Crater.
1018 *Geophysical Research Letters*, 49, e2021GL096920. doi:10.1029/2021GL096920
1019
1020 Irwin, R. P. III, Howard, A. D., Craddock, R. A., & Moore, J. M. (2005). An intense terminal
1021 epoch of widespread fluvial activity on early Mars: 2. Increased runoff and paleolake
1022 development. *Journal of Geophysical Research*, 110, E12S15. doi:10.1029/2005JE002460
1023
1024 Jodhpurkar, M. J., & Bell III, J. F. (2021). *Mapping and interpreting the northern fan deposit in*
1025 *Jezero crater, Mars*. Paper presented at the 52nd Lunar and Planetary Science Conference, The
1026 Woodlands, TX, Abstract #2252.
1027
1028 Kah, L., Scheller, E., Eide, S., Meyen, E., Jacob, S., Spaulding, R., et al. (2020). *Depositional*
1029 *relationships between crater floor materials in Jezero crater, Mars*. Paper presented at 51st
1030 Lunar and Planetary Science Conference, Houston, TX, Abstract #1301.
1031
1032 Kinch, K. M., Madsen, M. B., Bell III, J. F., Maki, J. N., Bailey, Z. J., Hayes, A. G., et al.
1033 (2020). Radiometric Calibration Targets for the Mastcam-Z Camera on the Mars 2020 Rover
1034 Mission. *Space Science Reviews*, 216, 141. doi:10.1007/s11214-020-00774-8

Kite, E. S. (2019). Geologic constraints on early Mars climate. *Space Science Reviews*, 215, 10. doi:10.1007/s11214-018-0575-5

Kremer, C. H., Mustard, J. F., & Bramble, M. S. (2019). A widespread olivine-rich ash deposit on Mars. *Geology*, 47, 677–681. doi:10.1130/G45563.1

Liu, Y., Tice, M. M., Schmidt, M. E., Treiman, A. H., Kizovski, T. V., Hurowitz, J. A., et al. (2022). An olivine cumulate outcrop on the floor of Jezero crater, Mars. *Science*, 377, 1513–1519. doi:10.1126/science.abo2756

Mandon, L., Quantin-Nataf, C., Thollot, P., Mangold, N., Lozac'h, L., Dromart, G., et al. (2020). Refining the age, emplacement and alteration scenarios of the olivine-rich unit in the Nili Fossae region, Mars. *Icarus*, 336, 113436. doi:10.1016/j.icarus.2019.113436

Mangold, N., Dromart, G., Ansan, V., Salese, F., Kleinhans, M. G., Massé, M., et al. (2020). Fluvial regimes, morphometry, and age of Jezero crater paleolake inlet valleys and their exobiological significance for the 2020 rover mission landing site. *Astrobiology*, 20, 994–1013. doi:10.1089/ast.2019.2132

Mangold, N., Gupta, S., Gasnault, O., Dromart, G., Tarnas, J. D., Sholes, S. F., et al. (2021). Perseverance rover reveals an ancient delta-lake system and flood deposits at Jezero crater, Mars. *Science*, 374, 711–717. doi:10.1126/science.abl4051

Marchi, S. (2021). A mew Martian crater chronology: Implications for Jezero crater. *The Astronomical Journal*, 161, 187. doi:10.3847/1538-3881/abe417

Maurice, S., Wiens, R. C., Bernardi, P., Caïs, P., Robinson, S., Nelson, T., et al. (2021). The SuperCam instrument suite on the Mars 2020 rover: Science objectives and Mast-Unit description. *Space Science Reviews*, 217, 1–108. doi:10.1007/s11214-021-00807-w

McBirney, A. R. (1996). The Skaergaard Intrusion. In R. G. Cawthorn (Ed.) Layered intrusions (pp. 147–180). Amsterdam: Elsevier.

McCallum, I. S. (1996). The Stillwater Complex. *Developments in Petrology*, 15, 441–483. doi:10.1016/S0167-2894(96)80015-7

Morris, R. V., Golden, D. C., Bell III, J. F., Lauer Jr, H. V., & Adams, J. B. (1993). Pigmenting agents in martian soils: Inferences from spectral, Mössbauer, and magnetic properties of nanophase and other iron oxides in Hawaiian palagonitic soil PN-9. Geochimica et Cosmochimica Acta, 57, 4597–4609. doi:10.1016/0016-7037(93)90185-Y

Mustard, J. F., Poulet, F., Gendrin, A., Bibring, J.-P., Langevin, Y., Gondet, B., et al. (2005). Olivine and pyroxene diversity in the crust of Mars. *Science*, 307, 1594–1597. doi:10.1126/science.1109098

Mustard, J. F., Ehlmann, B. L., Murchie, S. L., Poulet, F., Mangold, N., Head, J. W., et al. (2009). Composition, morphology, and stratigraphy of Noachian Crust around the Isidis basin. *Journal of Geophysical Research*, 114, E00D12. doi:10.1029/2009JE003349

Namur, O., Charlier, B., Toplis, M. J., Higgins, M. D., Liégeois, J-P., Vander Auwera, J. (2010). Crystallization sequence and magma chamber processes in the ferrobasaltic Sept Iles layered intrusion, Canada. Journal of Petrology, 51, 1203–1236. doi:10.1093/petrology/egq016

Namur, O., Abily, B., Boudreau, A. E., Blanchette, F., Bush, J. W. M., Ceuleneer, G., et al. (2015). Igneous layering in basaltic magma chambers. In B. Charlier, O. Namur, R. Latypov, and C. Tegner (Eds.), *Layered Intrusions* (pp. 75–152). Springer.

Núñez, J. I., Johnson, J. R., Horgan, B. N., Rice, M. S., Vaughan, A., Tate, C., et al. (2022). *Stratigraphy and mineralogy of the deposits within Séítah region on the floor of Jezero crater, Mars as seen with Mastcam-Z*. Paper presented at 53rd Lunar and Planetary Science Conference, The Woodlands, TX, Abstract #2937.

Osinski, G. R., Léveillé, R., Berinstain, A., Lebeuf, M., & Bamsey, M. (2006). Terrestrial analogues to Mars and the moon: Canada's role. *Geoscience Canada*, 33, 175–188.

Palumbo, A. M., Head, J. W., & Wilson, L. (2020). Rainfall on Noachian Mars: Nature, timing, and influence on geologic processes and climate history. *Icarus*, 347, 113782. doi:10.1016/j.icarus.2020.113782

Poulet, F., Mangold, N., Platevoet, B., Bardintzeff, J.-M., Sautter, V., Mustard, J. F., et al. (2009). Quantitative compositional analysis of Martian Mafic regions using the MEx/OMEGA reflectance data. *Icarus*, 201, 84–101. doi:10.1016/j.icarus.2008.12.042

Quantin-Nataf, C., Holm-Alwmark, S., Lasue, J., Calef, F. J., Shuster, D., Kinch, K. M., et al. (2021). The complex exhumation history of Jezero crater floor unit. Paper presented at 52nd Lunar and Planetary Science Conference, The Woodlands, TX, Abstract #2034.

Quantin-Nataf, C., Alwmark, S., Calef, F., Lasue, J., Kinch, K., Stack, K. M., et al. (this issue). The Complex Exhumation History of Jezero Crater Floor Unit and its implication for Mars Sample return.

Ravanis, E., Fagents, S., Newman, C., Horgan, B., Holm-Alwmark, S., Brown, A. J., et al. (2022). The potential for pyroclastic deposits in the Jezero crater region of Mars from ash dispersal modeling. Paper presented at 53rd Lunar and Planetary Science Conference, The Woodlands, TX, Abstract #1692.

Rice, M. S., Johnson, J. R., Million, C. C., St. Clair, M., Horgan, B. N., Vaughan, A., et al. (2022a). *Summary of Mastcam-Z visible to near infrared (VNIR) multispectral observations from Perseverance's mission in Jezero crater, Mars*. Paper presented at 53rd Lunar and Planetary Science Conference, The Woodlands, TX, Abstract #2559.

1127 Rice, M. S., Johnson, J. R., Million, C. C., St. Clair, M., Horgan, B. N., et al. (2022b). Mastcam-
1128 Z multispectral database from the Perseverance rover's traverse in the Jezero crater floor, Mars
1129 (sols 0-380). WWU Geology Faculty Publications, 105. doi:10.25710/bhyk-kc32
1130
1131 Robbins, S. J., Achille, G. D., & Hynek, B. M. (2011). The volcanic history of Mars: High-
1132 resolution crater-based studies of the calderas of 20 volcanoes. *Icarus*, 211, 1179–1203.
1133 doi:10.1016/j.icarus.2010.11.012
1134
1135 Rowland, S. K., & Walker, G. P. L. (1990). Pāhoehoe and aa in Hawaii: Volumetric flow rate
1136 controls the lava structure. *Bulletin of Volcanology*, 52, 615–628. doi:10.1007/BF00301212
1137
1138 Ruff, S. W. (2017). *Investigating the floor of paleolake Jezero by way of Gusev crater*. Paper
1139 presented at the Fourth International Conference on Early Mars. Flagstaff, AZ, Abstract #3076.
1140
1141 Salese, F., McMahon, W. J., Balme, M. R., Ansan, V., Davis, J. M., & Kleinhans, M. G. (2020).
1142 Sustained fluvial deposition recorded in Mars' Noachian stratigraphic record. *Nature*
1143 *Communications*, 11, 2067. doi:10.1038/s41467-020-15622-0
1144
1145 Schmidt, M. E., Allwood, A., Christian, J., Clark, B. C., Flannery, D., Hennecke, J., et al. (2022).
1146 *Highly differentiated basaltic lavas examined by PIXL in Jezero crater*. Paper presented at 53rd
1147 Lunar and Planetary Science Conference, The Woodlands, TX, Abstract #1530.
1148

1149 Schon, S. C., Head, J. W., & Fassett, C. I. (2012). An overfilled lacustrine system and
1150 progradational delta in Jezero crater, Mars: Implications for Noachian climate. *Planetary and*
1151 *Space Science*, 67, 28–45. doi:10.1016/j.pss.2012.02.003
1152
1153 Self, S., Mittal, T., & Jay, A. E. (2021) Thickness characteristics of pāhoehoe lavas in the
1154 Deccan Province, Western Ghats, India, and in continental flood basalt provinces elsewhere.
1155 Frontiers in Earth Science, 8. doi:10.3389/feart.2020.630604
1156
1157 Shahrzad, S., Kinch, K. M., Goudge, T. A., Fassett, C. I., Needham, D. H., Quantin-Nataf, C., &
1158 Knudsen, C. P. (2019). Crater statistics on the dark-toned, mafic floor unit in Jezero crater, Mars.
1159 *Geophysical Research Letters*, 46, 2408–2416. doi:10.1029/2018GL081402
1160
1161 Sheth, H. C. (2006) The emplacement of pāhoehoe lavas on Kilauea and in the Deccan traps.
1162 Journal of Earth System Science, 115, 615–629. doi:10.1007/s12040-006-0007-x
1163
1164 Simon, J. I., Amundsen, H. E. F., Beegle, L. W., Bell III., J. F., Benison, K. C., Berger, E. L., et
1165 al. (2022). Sampling of Jezero crater Máaz formation by Mars 2020 Perseverance rover. Paper
1166 presented at 53rd Lunar and Planetary Science Conference, The Woodlands, TX, Abstract #1294.
1167
1168 Simon, J. I., et al. (this issue). Samples Collected from the Floor of Jezero Crater with the Mars
1169 2020 Perseverance Rover, this issue.
1170

1171 Skilling, I. P. (2002). Basaltic pāhoehoe lava-fed deltas: large-scale characteristics, clast
1172 generation, emplacement processes and environmental discrimination. Geological Society,
1173 London, Special Publications, 202, 91–113. doi: 10.1144/GSL.SP.2002.202.01.06
1174
1175 Stack, K. M., Williams, N. R., Calef, F. J. III, Sun, V. Z., Williford, K. H., Farley, K. A., et al.
1176 (2020). Geology of the Mars 2020 landing site, Jezero crater, Mars: Insights from photo-geologic
1177 mapping by the Mars 2020 science team. *Space Science Reviews*, 216, 127. doi:10.1007/s11214-
1178 020-00739-x
1179
1180 Sun, V. Z., & Stack, K. M. (2020a). *Geologic map of Jezero Crater and the Nili Planum region,*
1181 *Mars* (Map pamphlet 14 p., 1 sheet, scale 1:75,000). U.S. Geological Survey Scientific
1182 Investigations. doi:10.3133/sim3464
1183
1184 Sun, V. Z., & Stack, K. M. (2020b). *Geologic map of the Jezero and Nili Planum regions of*
1185 *Mars 2020*. Paper presented at Annual Meeting of Planetary Geologic Mappers, Abstract #7019.
1186
1187 Sun, V. Z., Hand, K. P., Stack, K. M., Farley, K. A., Milkovich, S., Kronyak, R., et al. (2022).
1188 *Exploring the Jezero crater floor: Overview of results from the Mars 2020 Perseverance rover's*
1189 *first science campaign*. Paper presented at 53rd Lunar and Planetary Science Conference, The
1190 Woodlands, TX, Abstract #1798.
1191

1192 Sun, V. Z., Hand, K. P., Stack, K. M., Farley, K. A., Simon, J. I., Newman, C., et al. (this issue).
1193 Overview and results from the Mars 2020 Perseverance rover's first science campaign on the
1194 Jezero crater floor.
1195
1196 Udry, A., et al. (this issue). A Mars 2020 Perseverance SuperCam perspective on the igneous
1197 nature of the Máaz formation at Jezero crater and link with Séítah, Mars. This issue.
1198
1199 Udry, A., Sautter, V., Cousin, A., Wiens, R. C., Forni, O., Benzerara, K., et al. (2022). *A Mars*
1200 *2020 Perseverance SuperCam perspective on the igneous nature of the Máaz formation at Jezero*
1201 *crater, Mars*. Paper presented at 53rd Lunar and Planetary Science Conference, The Woodlands,
1202 TX, Abstract #2257.
1203
1204 Vaughan, A., Minitti, M. E., Cardarelli, E. L., Johnson, J. R., Kah, L. C., Pilleri, P., et al. (this
1205 issue). Regolith of the crater floor units, Jezero crater, Mars: Textures, composition and
1206 implications for provenance. This issue.
1207
1208 Voigt, J. R. C, Hamilton, C. W., Scheidt, S. P., Münzer, U., Höskuldsson, Á, Jónsdottir, I., et al.
1209 (2021). Geomorphological characterization of the 2014–2015 Holuhraun lava flow-field in
1210 Iceland. *Journal of Volcanology and Geothermal Research*, 419, 107278. doi:
1211 10.1016/j.jvolgeores.2021.107278
1212
1213 Werner, S. C. (2008). The early Martian evolution—Constraints from basin formation ages.
1214 *Icarus*, 195, 45–60. doi:10.1016/j.icarus.2007.12.008

White, J. D., McPhie, J., & Soule, S. A. (2015). Submarine lavas and hyaloclastite. In H. Sigurdsson, B. Houghton, S. McNutt, H. Rymer, & J. Stix (Eds.), *The Encyclopedia of Volcanoes* (pp. 363–375). Academic Press.

Wiens, R. C., & Maurice, S. A. (2021). Mars 2020 SuperCam Bundle. NASA Planetary Data System. doi:10.17189/1522646

Wiens, R. C., Maurice, S., Robinson, S. H., Nelson, A. E., Caïs, P., Bernardi, P., et al. (2021). The SuperCam instrument suite on the NASA Mars 2020 rover: Body unit and combined system tests. *Space Science Reviews*, 217:1–87. doi:10.1007/s11214-020-00777-5

Wiens, R. C., Udry, A., Beyssac, O., Quantin-Nataf, C., Mangold, N., Cousin, A., et al. (2022). Compositionally and density stratified igneous terrain in Jezero crater, Mars. *Science Advances*, 8, eabo3399. doi: 10.1126/sciadv.abo339

Figure Captions

Figure 1. a) Color-coded elevation (in m) overview image of Jezero crater based on the High Resolution Imaging Science Experiment (HiRISE) digital elevation model and corresponding orthoimages (modified after Holm-Alwmark et al., 2021). **b)** Enlarged view of area of interest with Máaz and Séítah formation rocks and rover traverse in black. White dashed line indicates approximate division between the Máaz and Séítah formations. Basemap is HiRISE color image (Fergason et al., 2020). **c)** View of upper Máaz formation Ch'ał member rocks overlaying the Naat'áanii member pavers near the Octavia E. Butler landing site. This enhanced color Mastcam-Z mosaic was obtained on sol 369 at a focal length of 34 mm. Credit: NASA/JPL-Caltech/ASU/MSSS/K. Powell. Numbers along borders of mosaics are azimuth and elevation coordinates (in relation to rover position when images were obtained). **d)** Stratigraphic profile

and members of the Séítah and Máaz formations (based on Crumpler et al., this issue; Horgan et al., this issue; Sun et al., this isse).

Figure 2. a) Magnified view of the Artuby ridge with outcrops, workspaces, and samples relevant to this study indicated by numbers. For full list of targets analyzed see Table S1. Basemap is HiRISE IRB color (Fergason et al., 2020) from CAMP (e.g., Stack et al., 2020). **b)** Mastcam-Z sol 173 enhanced color mosaic of Artuby ridge at a focal length of 110 mm. Credit: NASA/JPL-Caltech/ASU/MSSS/C. Rojas. **c)** Mastcam-Z sol 174 enhanced color mosaic of Artuby ridge with the Artuby_116 outcrop at a focal length of 63 mm. Credit: NASA/JPL-Caltech/ASU/MSSS/L. Mehall. **d)** Mastcam-Z sol 305 enhanced color mosaic of the Séítah-Máaz transition from Lombards to Artuby ridge at a focal length of 34 mm. Credit: NASA/JPL-Caltech/ASU/MSSS/K. Powell.

Figure 3. Enlarged views of the Artuby_116 and Rimplas outcrops at the Artuby ridge. **a)** Mastcam-Z left eye sol 175 image of the Artuby_116 outcrop at a focal length of 63 mm. The whole outcrop section in this view is approximately 3 m in height. **b)** Enlarged view of knobbly layers in the Artuby_116 outcrop. **c)** Mastcam-Z sol 342 enhanced color mosaic at a focal length of 110 mm that shows the Artuby_116 outcrop and the Rimplas workspace to the left. Marked on this image with numbers 1 and 2 are the two sections where we have measured layer thicknesses (see main text). Credit: NASA/JPL-Caltech/ASU/MSSS/L. Mehall. **d)** Mastcam-Z sol 177 enhanced color mosaic of the Grasse outcrop at Artuby_116, taken at a focal length of 110 mm. Credit: NASA/JPL-Caltech/ASU/MSSS/K. Powell. **e)** Mastcam-Z left eye image obtained on sol 342 at a focal length of 110 mm showing both bulbous morphologies and quasi-planar layers at the Artuby_116 outcrop. **f)** Mastcam-Z sol 175 enhanced color mosaic of bulbous layers at Artuby ridge (Artuby_116 outcrop) at a focal length of 110 mm. Credit: NASA/JPL-Caltech/ASU/MSSS/L. Mehall. **g)** Enlarged view of bulbous morphologies of layers at the Artuby ridge. Arrows point to places where layers appear to have flowed over underlying strata, and where individual lobes pinch out. Mastcam-Z right eye image obtained on sol 175 at a focal length of 110 mm. **h)** Mastcam-Z sol 343 enhanced color mosaic of the Rimplas workspace at Artuby ridge, taken at a focal length of 110 mm. Note that the knobbly layers have internal foliation which is not as evident on knobs that are less weathered (right side of image). Credit: NASA/JPL-Caltech/ASU/MSSS/K. Powell.

Figure 4. a) Mastcam-Z sol 292 enhanced color mosaic of part of the Artuby West ridge at a focal length of 34 mm. Credit: NASA/JPL-Caltech/ASU/MSSS/L. Mehall. **b)** Mastcam-Z right eye image of layers on Artuby West ridge obtained on sol 292 at a focal length of 110 mm. **c)** Cropped section of Mastcam-Z left eye image obtained on sol 288 of layers on Artuby West ridge at a focal length of 110 mm. Note what could be overlapping flow lobes (arrow) on the right side of the regolith-covered crevasse. Or alternatively, that the top layer appears to have slumped, or flowed, over underlying strata. **d)** Mastcam-Z left eye image obtained on sol 288 of layers on Artuby West ridge at a focal length of 110 mm.

Figure 5. Schematic stratigraphy of the Artuby ridge and examples of the various morphologies and surface textures of Artuby ridge targets, with hypotheses for formation of strata summarized. **a)** Schematic and simplified statigraphic column of the Artuby_116 outcrop at Artuby ridge. Letters refer to where RMIs targets in b, c, and d correspond to in stratigraphy. Sections with

numbers 1 and 2 correspond roughly to where layer thickness have been measured (see also Fig. 3c). **b)** SuperCam RMI of target Amirat obtained on sol 290. **c)** SuperCam RMI of target Majastres obtained on sol 294. **d)** SuperCam RMI of target Grasse obtained on sol 177.

Figure 6. Magnesium number and major element compositions (SiO_2+Al_2O_3) of SuperCam targets on the Artuby ridge (light gray circles), and targets located off the ridge (see Fig. 2a) that are, or may be, in Séítah stratigraphy (dark gray circles).

Figure 7. Summary of Mastcam-Z multispectral data from Artuby ridge. **a)** Plot of all high-quality spectra extracted from Artuby ridge, comparing spectral slopes at long and short wavelengths with 525 nm band depth. All three parameters are high for ferric oxides, but vary for ubiquitous purple coatings and exposed rock. Squares indicate Artuby member observations and circles indicate Rochette member observations, which follow similar patterns. **b)** Representative Mastcam-Z spectra, displaying the similarity between Artuby member knobs, resistant Rochette member cap rocks, and local regolith.

Figure 8. Examples of complex layers, foliations, and fractures in the interior of lava flows over a range of morphologies, compositions, and viscosities. **a)** Typical inflated pāhoehoe lava section with massive interior and vesicular upper and lower sections. Note sub-orthogonal joints in upper section. Laguna lava flow, New Mexico. **b)** Typical ʻaʻā lava section with foliated basal zone and chaotic interior fractures. Sub-alkaline basalt, Cerros del Rio volcanic field, west of Santa Fe, New Mexico. **c)** Shearing foliations within the massive interior of a trachybasalt lava section. Mt. Taylor volcano, New Mexico. **d)** Basal structure of an ʻaʻā trachybasalt lava flow, note the relatively vesicle-free and massive interior underlain by a scoriaceous basal breccia. The basal scoria results from combined over-riding of brittle chill zone fragments, basal initial melt vesicularity, and local pyroclastic fallout. Mt. Taylor volcanic field, New Mexico. **e)** Inflated tholeiitic pāhoehoe flow section with interior late-stage tube-like ellipsoidal zone. Note orthogonal jointing in upper section. McCartys lava flow, New Mexico. **f)** Basal shear foliations at the base of a thick massive, columnar zone within a porphyritic trachyandesite lava flow. Mt. Taylor volcano, New Mexico.

Figure 9. Photographs of volcanic terrestrial analog sites compared to morphologies of the Artuby ridge. **a)** Bulbous textures in weathered/exposed stack of pāhoehoe lobes on Oahu. **b)** Blocky lava outcrop atop laterally discontinuous pāhoehoe lobes on Oahu. **c)** Road cut through a stack of flows on Oahu. **d)** Magnified view of the same flow stack as in a), highlighting the variable friability of the layers and the complex lobe/intraflow textures with relatively fine-scale foliation.

Figure 1.

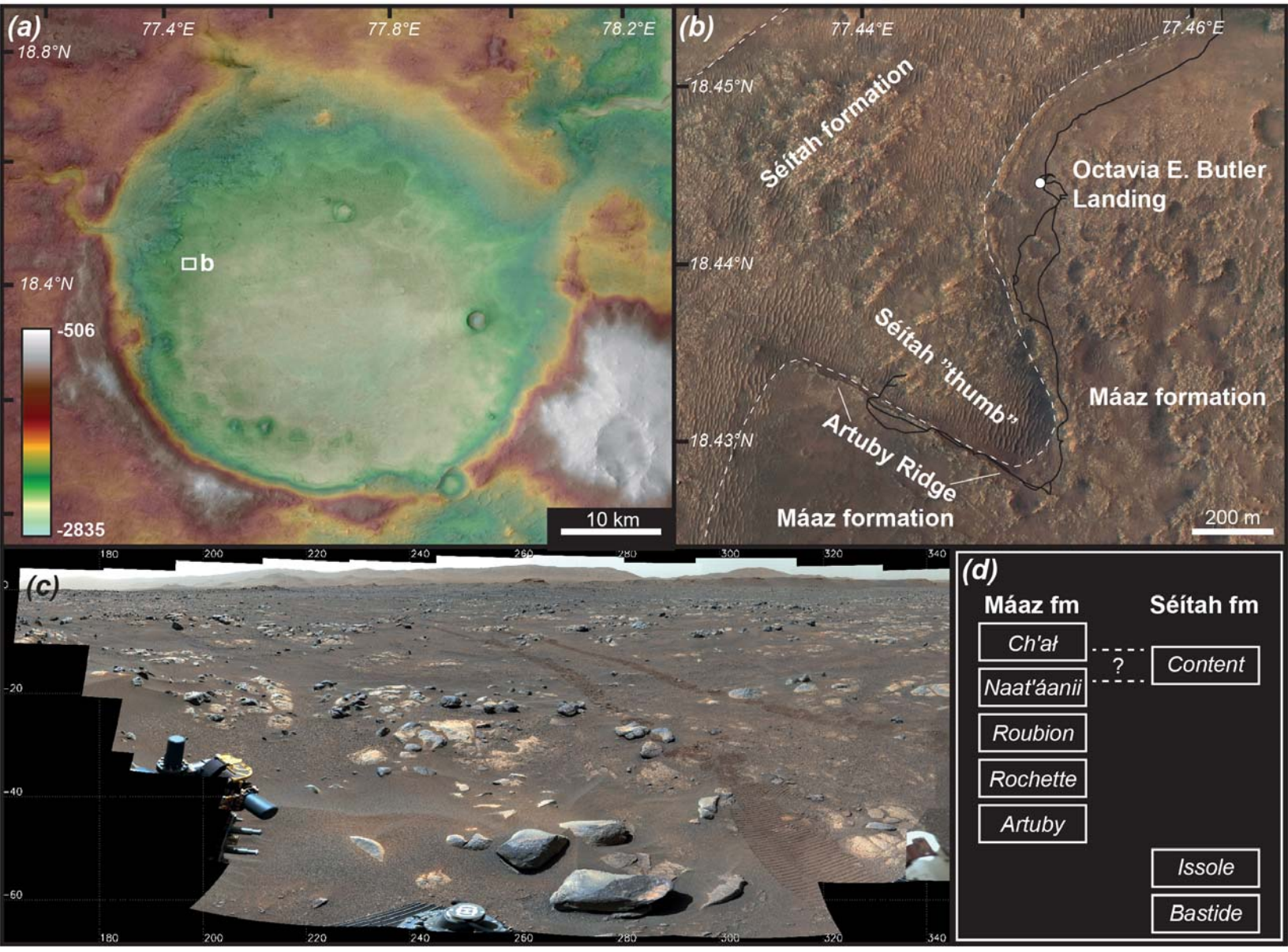
(a)
77.4°E
77.8°E
78.2°E
18.8°N
18.4°N
b
-506
-2835
10 km
(b)
77.44°E
77.46°E
18.45°N
18.44°N
18.43°N
Séítah formation
Octavia E. Butler Landing
Séítah "thumb"
Máaz formation
Artuby Ridge
Máaz formation
200 m
(c)
180
200
220
240
260
280
300
320
340
-20
-40
-60
(d)
Máaz fm
Séítah fm
Ch'ał
Naat'áanii
Roubion
Rochette
Artuby
?
Content
Issole
Bastide

Figure 2.

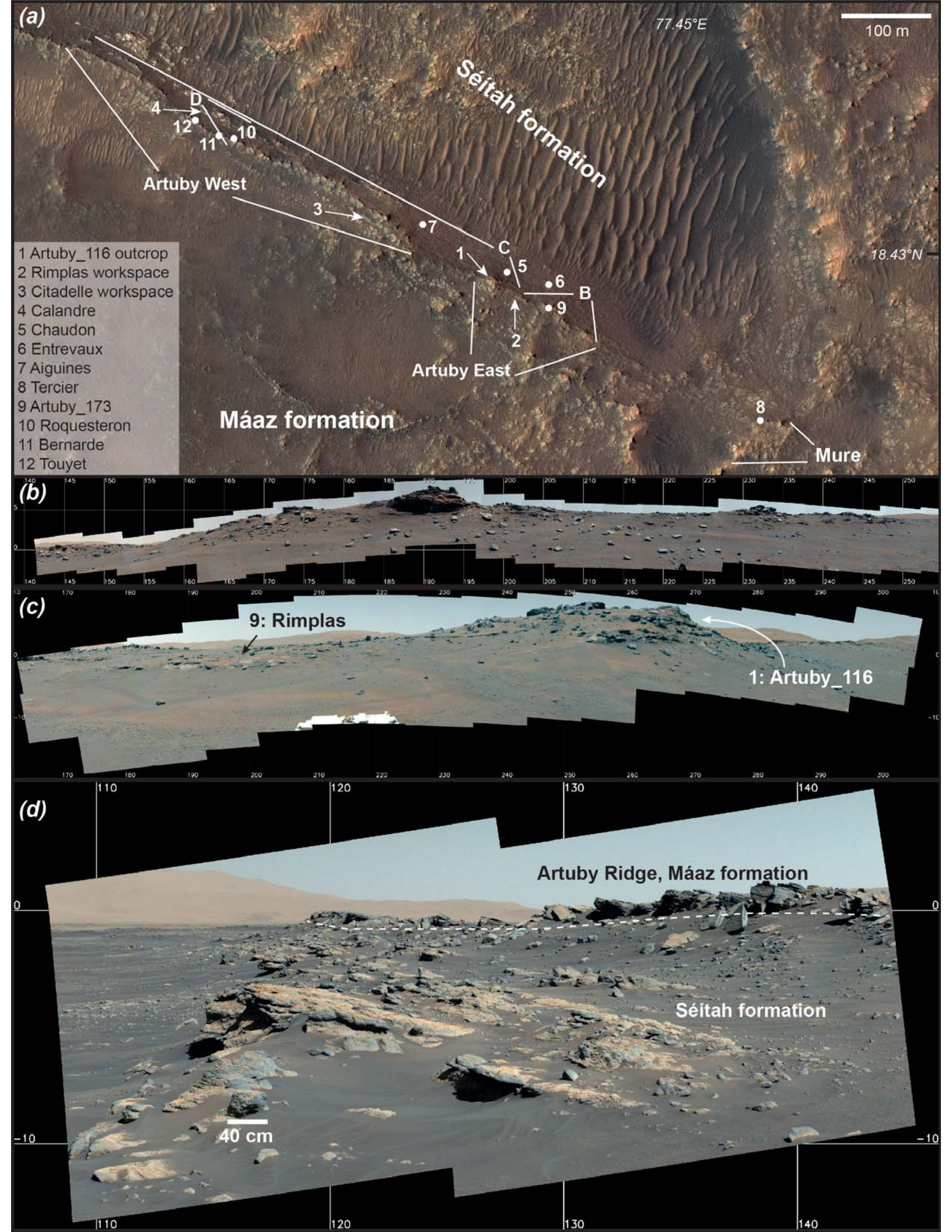
(a)
77.45°E
100 m
18.43°N
Séítah formation
Artuby West
Artuby East
Máaz formation
Mure
D
C
B
1 Artuby_116 outcrop
2 Rimplas workspace
3 Citadelle workspace
4 Calandre
5 Chaudon
6 Entrevaux
7 Aiguines
8 Tercier
9 Artuby_173
10 Roquesteron
11 Bernarde
12 Touyet
(b)
(c)
9: Rimplas
1: Artuby_116
(d)
Artuby Ridge, Máaz formation
Séítah formation
40 cm

Figure 3.

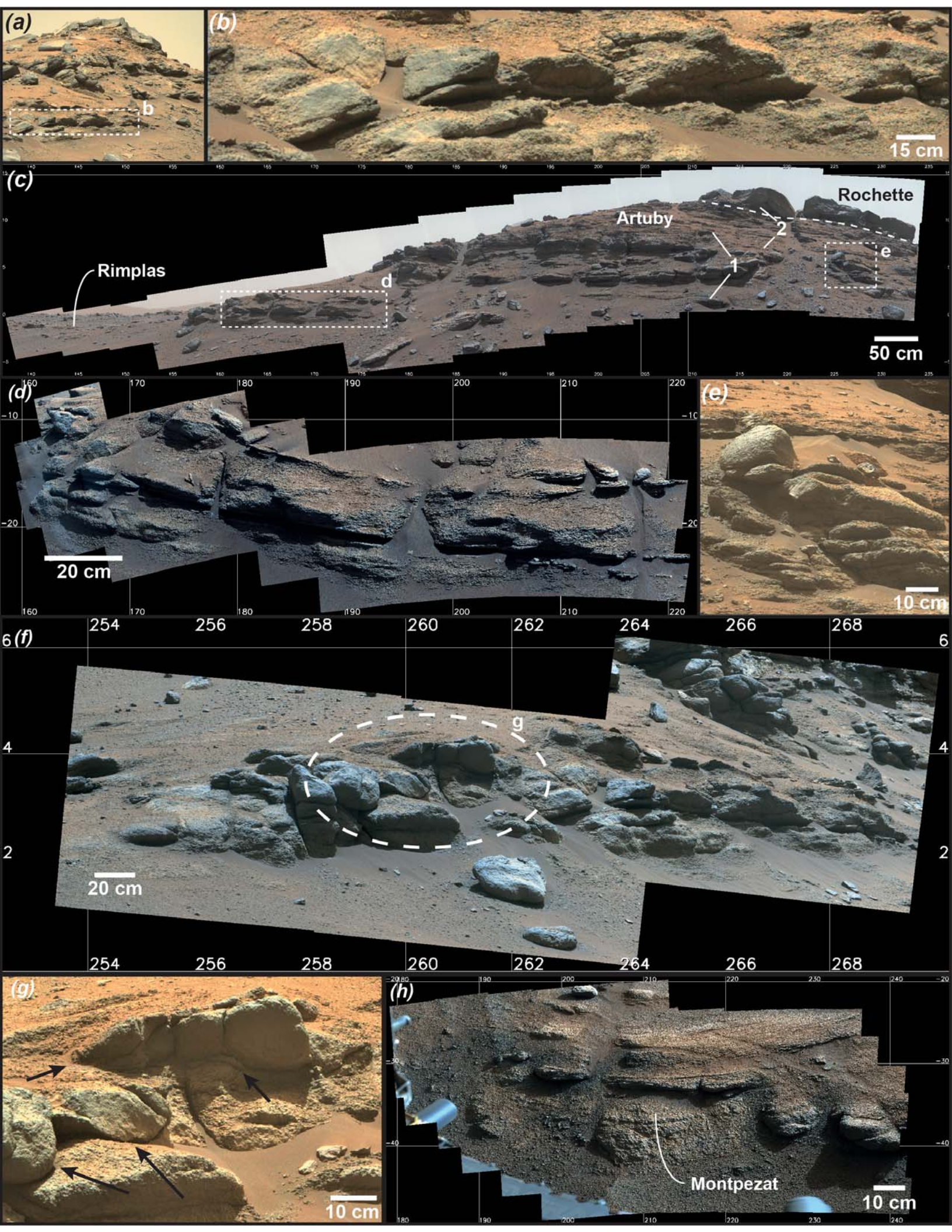
(a)
b
(b)
15 cm
(c)
Rochette
Artuby
2
1
e
Rimplas
d
50 cm
(d)
20 cm
(e)
10 cm
(f)
g
20 cm
(g)
10 cm
(h)
Montpezat
10 cm

Figure 4.

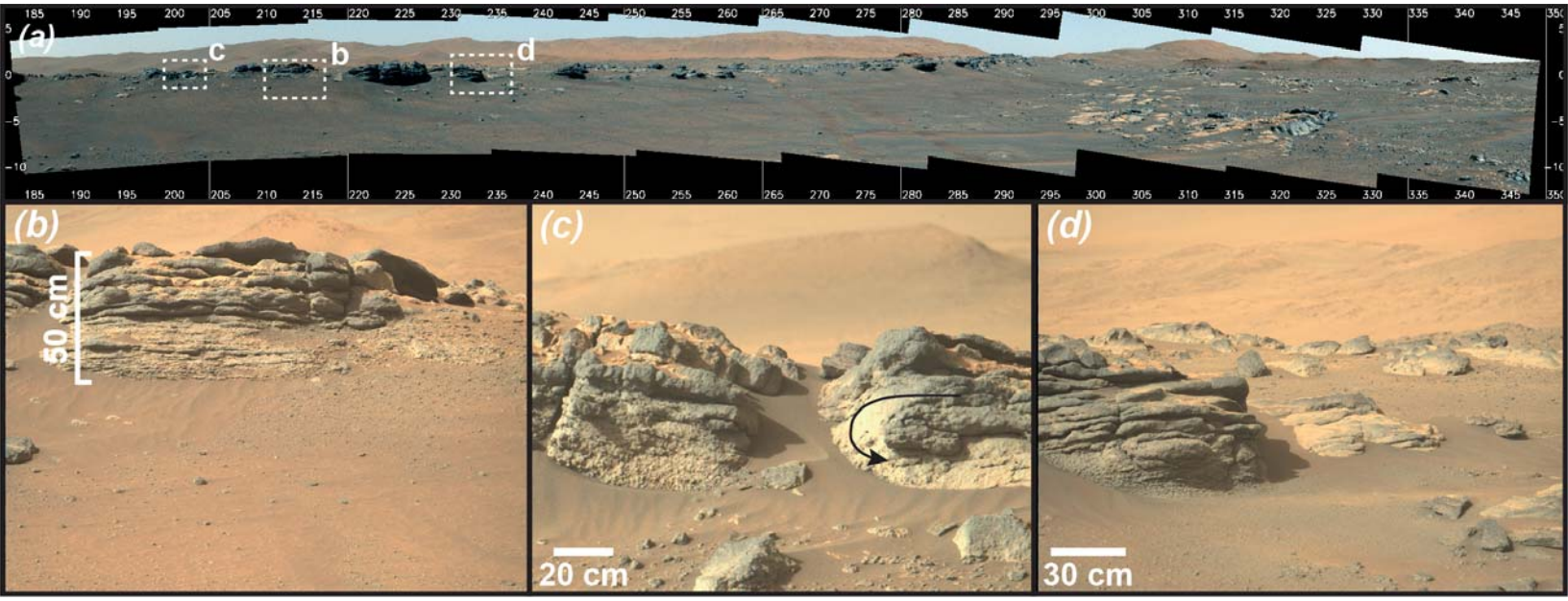
(a)
c
b
d
(b)
50 cm
(c)
20 cm
(d)
30 cm

Figure 5.

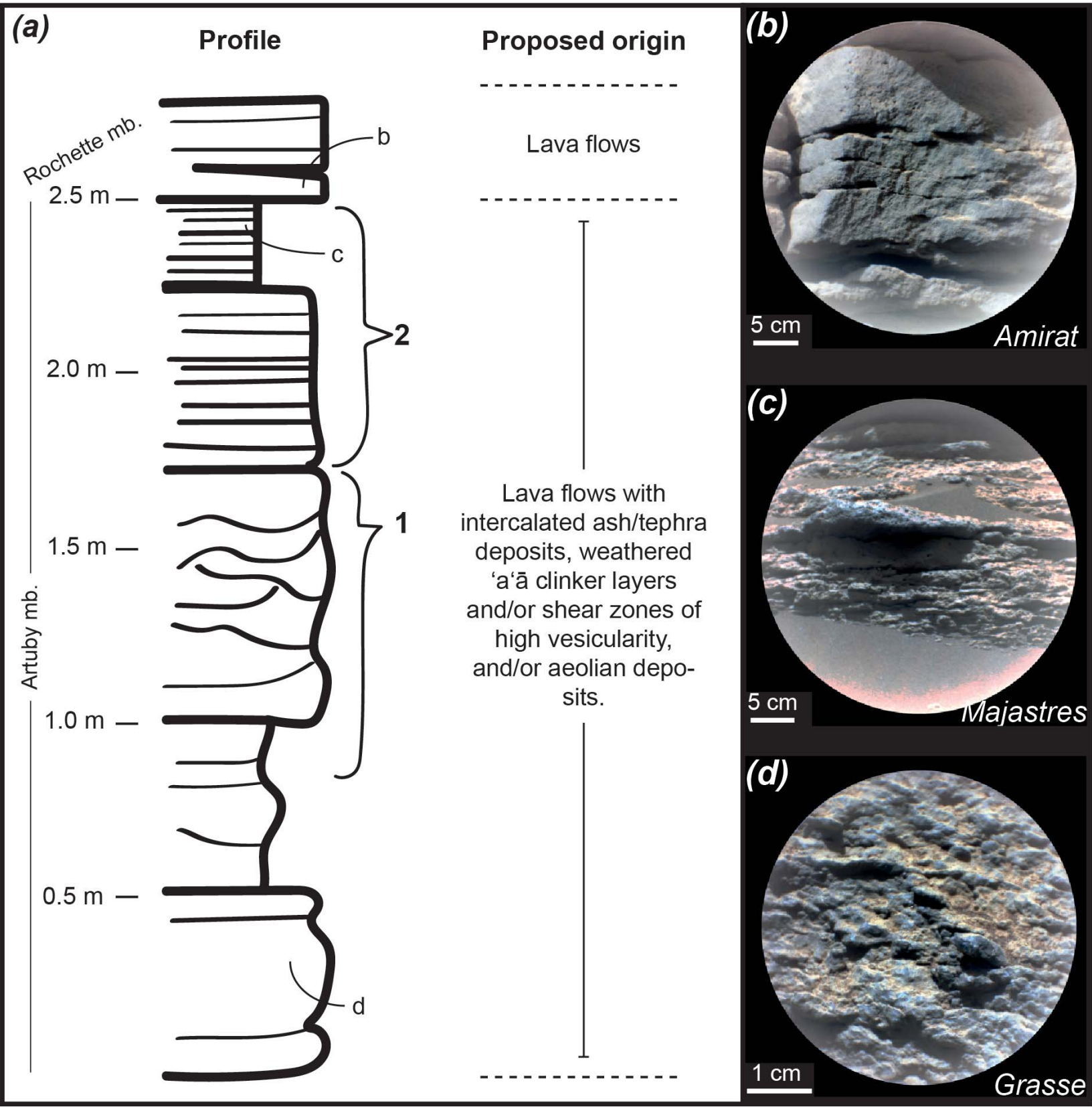
(a)
Profile
Proposed origin
Rochette mb.
Artuby mb.
2.5 m
2.0 m
1.5 m
1.0 m
0.5 m
b
c
d
2
1
Lava flows
Lava flows with intercalated ash/tephra deposits, weathered ‘a‘ā clinker layers and/or shear zones of high vesicularity, and/or aeolian depo-sits.
(b)
5 cm
Amirat
(c)
5 cm
Majastres
(d)
1 cm
Grasse

Figure 6.

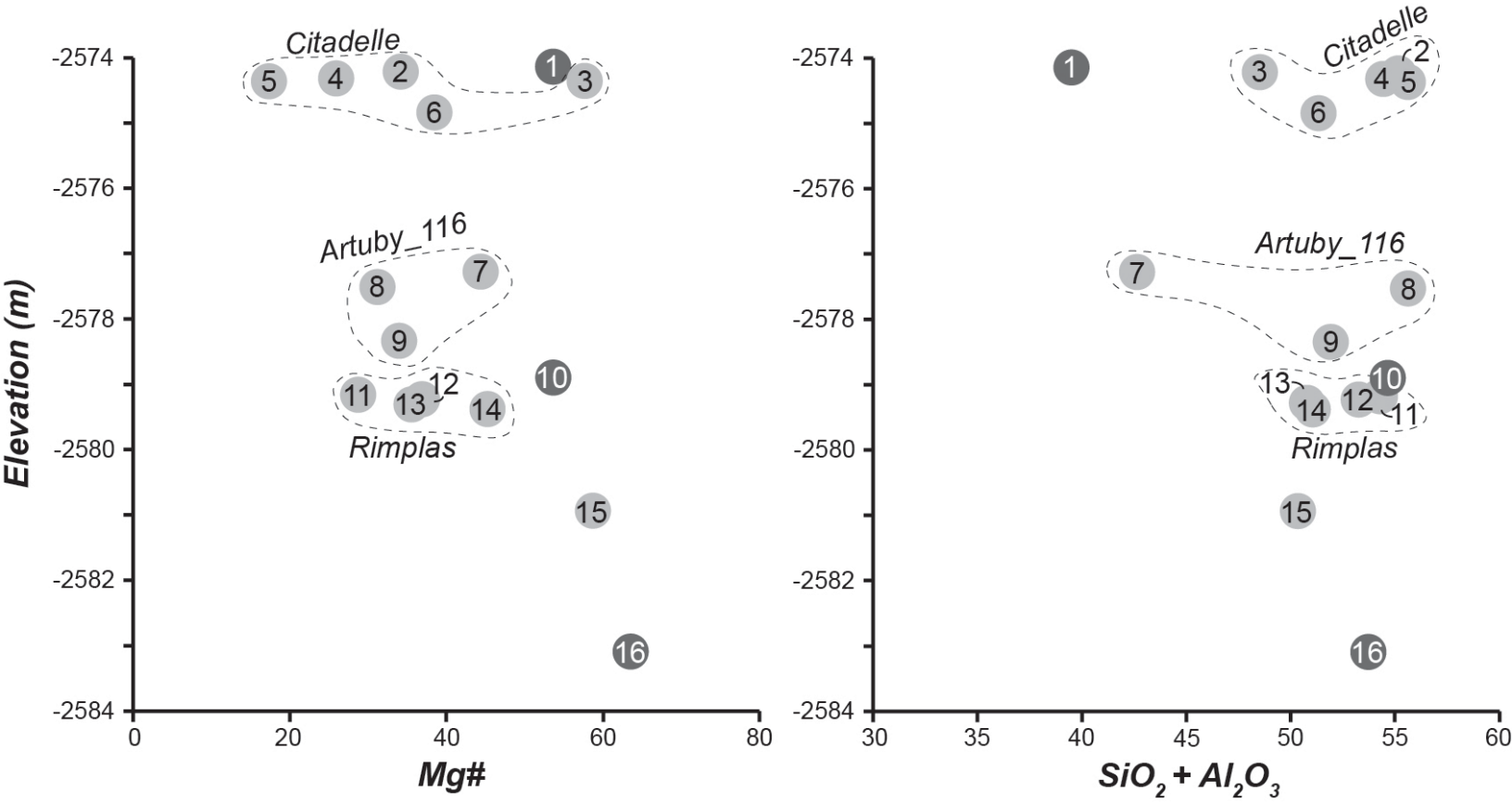

(1) Calandre, (2) Sauzeries_Haute, (3) Grandes_Tours_du_Lac, (4) Estoublon, (5) Manior, (6) Rigaud, (7) Vaucluse, (8) Auribeau, (9) Grasse, (10) Aiguines, (11) Blache, (12) Vergons, (13) Montpezat, (14) Galabre, (15) Chaudon, (16) Entrevaux

Figure 7.

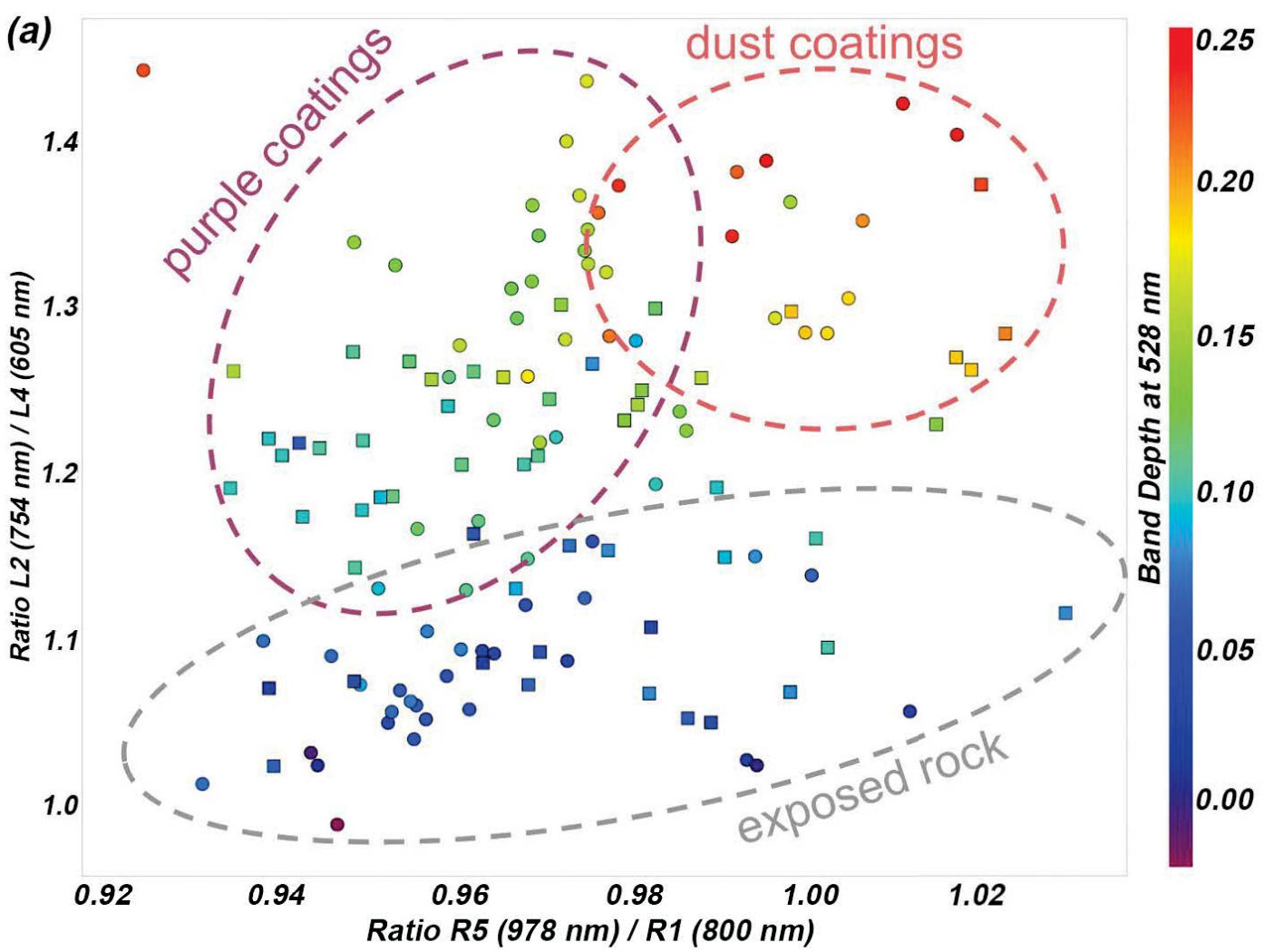
(a)
purple coatings
dust coatings
exposed rock
Ratio L2 (754 nm) / L4 (605 nm)
Ratio R5 (978 nm) / R1 (800 nm)
Band Depth at 528 nm
1.0
1.1
1.2
1.3
1.4
0.92
0.94
0.96
0.98
1.00
1.02
0.00
0.05
0.10
0.15
0.20
0.25

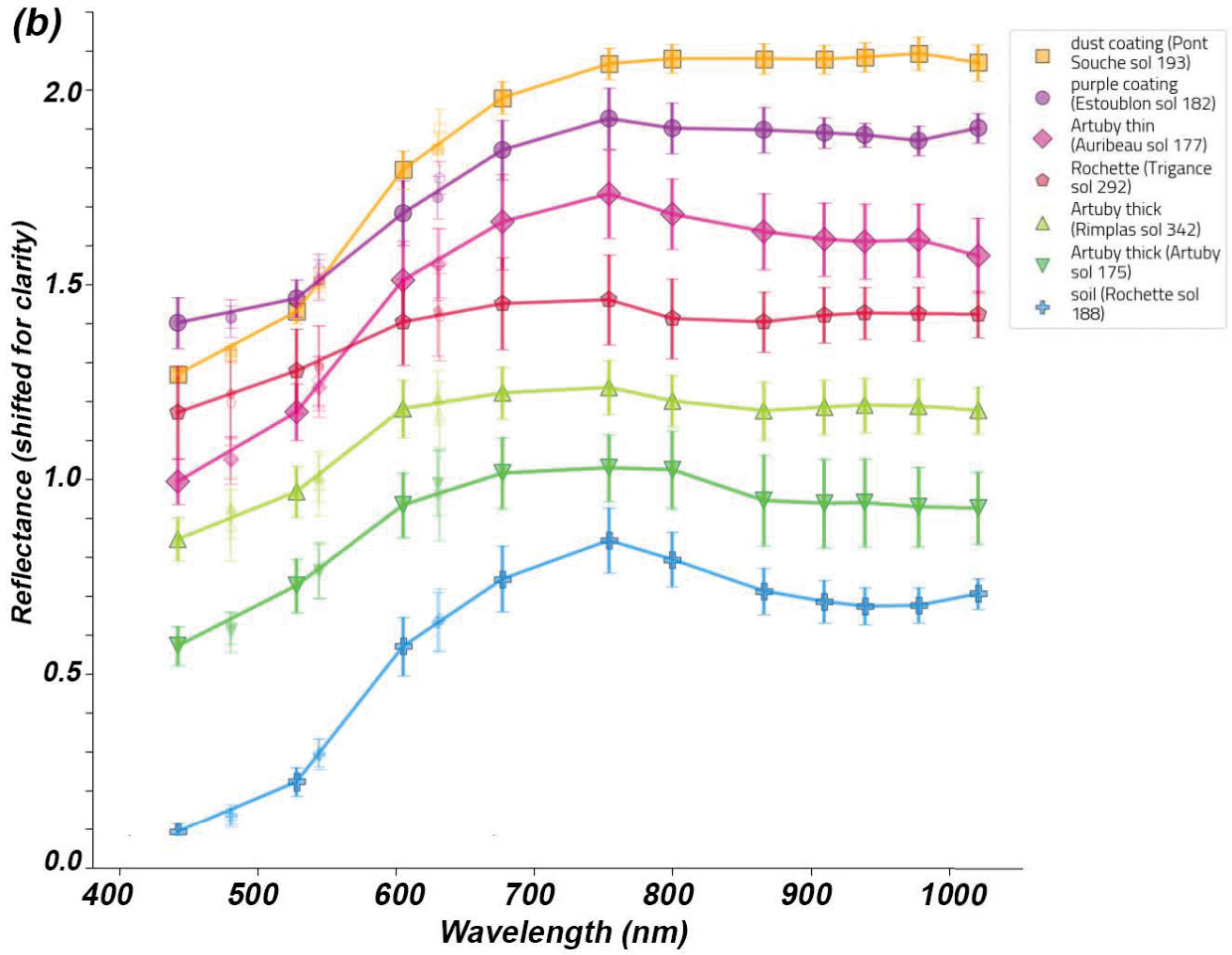
(b)
Reflectance (shifted for clarity)
Wavelength (nm)
0.0
0.5
1.0
1.5
2.0
400
500
600
700
800
900
1000
dust coating (Pont Souche sol 193)
purple coating (Estoublon sol 182)
Artuby thin (Auribeau sol 177)
Rochette (Trigance sol 292)
Artuby thick (Rimplas sol 342)
Artuby thick (Artuby sol 175)
soil (Rochette sol 188)

Figure 8.

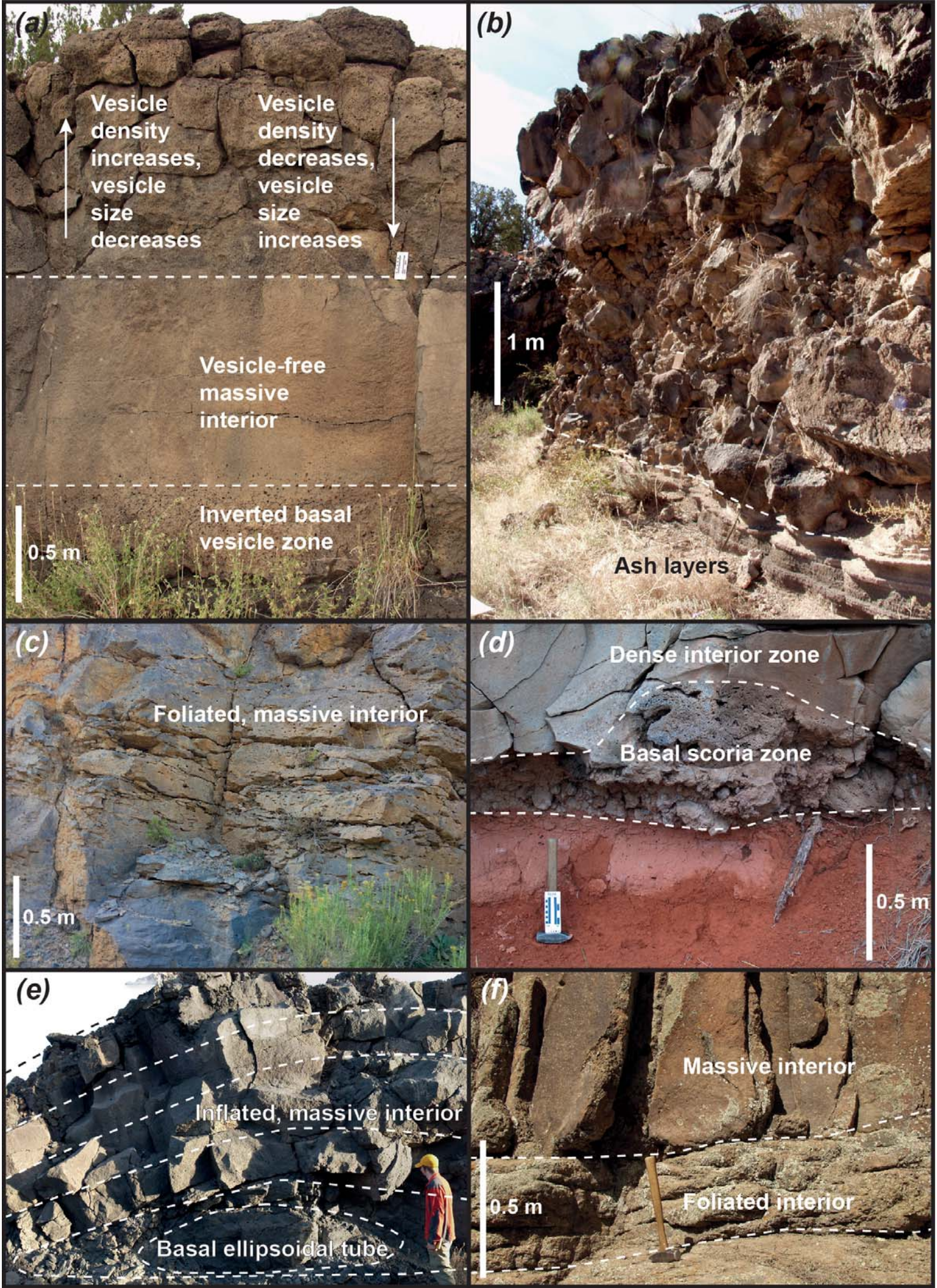
(a)
Vesicle density increases, vesicle size decreases
Vesicle density decreases, vesicle size increases
Vesicle-free massive interior
Inverted basal vesicle zone
0.5 m
(b)
1 m
Ash layers
(c)
Foliated, massive interior
0.5 m
(d)
Dense interior zone
Basal scoria zone
0.5 m
(e)
Inflated, massive interior
Basal ellipsoidal tube
(f)
Massive interior
0.5 m
Foliated interior

Figure 9.


(a)
1 m
Bulbous morphology
(b)
20 cm
(c)
3 m
(d)
1 m